



Experimental Investigation of Spalling Failure of D-Shaped Tunnel Under Three-Dimensional High-Stress Conditions in Hard Rock

Xuefeng Si¹ · Linqi Huang¹ · Xibing Li¹ · Chunde Ma¹ · Fengqiang Gong^{1,2}

Received: 9 January 2020 / Accepted: 14 October 2020 / Published online: 5 November 2020
© Springer-Verlag GmbH Austria, part of Springer Nature 2020

Abstract

The D-shaped cross section is a commonly used tunnel cross section in underground engineering. To simulate the failure process of a D-shaped hole under deep three-dimensional (3D) high-stress conditions, true-triaxial tests were conducted on cubic granite specimens with a through D-shaped hole, and the failure process of the hole sidewall was recorded in real time. Results show that the spalling failure process of the D-shaped hole sidewall can be divided into four periods: calm, fine particle ejection, crack generation and propagation, and rock slab gradually buckling and spalling. Afterwards, symmetrical V-shaped notches were formed on both sidewalls between the corner and arch springing. The spalling failure shows tensile failure characteristics. Under high vertical stress and constant horizontal axial stress, increasing the lateral stress reduces the severity of the spalling failure and the depth of the V-shaped notch. The initial failure vertical stress of the D-shaped hole sidewall is higher than that of circular hole sidewall, and the failure of D-shaped hole sidewall is mainly characterized by static failure. The failure of the circular hole sidewall is a more severe dynamic failure. When the vertical applied stress is the maximum principal stress, the position of the V-shaped notch tip is 0.20–0.25 h (h is the height of the D-shaped tunnel) from the tunnel floor, whereas that in the circular tunnel is 0.5 d (d is the diameter of the circular tunnel) from the tunnel floor. Specific support schemes should therefore be designed for tunnels with different cross sections according to the damage location, depth of failure zone, and severity of failure.

Keywords Deep D-shaped tunnel · Spalling failure · True-triaxial test · Three-dimensional high-stress · V-shaped notch

List of Symbols

d Diameter of the circular tunnel
 h Height of the D-shaped tunnel

Greek Symbols

$\sigma_{h\max}, \sigma_{h\min}$ Maximum horizontal geostress and minimum horizontal geostress
 σ_v Vertical geostress
 $\sigma_X, \sigma_Y, \sigma_Z$ Horizontal axial stress, lateral stress, and vertical stress

Abbreviations

3D Three-dimensional
CT Computed tomography
ISRM International Society for Rock Mechanics

1 Introduction

Many types of tunnel cross section shapes are used in underground engineering. The D-shaped cross section is one of the commonly used tunnel cross sections. Under the action of deep high-stress, spalling failure often occurs in tunnel surrounding rock (Dowding and Andersson 1986; Ortlepp and Stacey 1994; Martin et al. 1997; Martin 1997; Diederichs 2007; Gong et al. 2012; Jiang et al. 2017; Luo 2020; Luo et al. 2020), which adversely affects the supporting structure of tunnels and threatens the safety of the underground construction and equipment (Zhou et al. 2016; Feng et al. 2018). Spalling failure typically occurs approximately parallel to the maximum principal stress direction (Cai et al. 1998, 2008; Jia et al. 2012).

To study the mechanism of rock spalling failure, many researchers have carried out studies on the spalling failure of rock materials (Pinto and Fonseca 2013; Qiu et al. 2014; Du et al. 2016; Li et al. 2017, 2018a; Wang et al. 2020). Pinto and Fonseca (2013) determined that the destruction process of granite and other rocks under uniaxial compressive loading includes two periods: (1) the formation of

✉ Linqi Huang
huanglinqi@csu.edu.cn

¹ School of Resources and Safety Engineering, Central South University, Changsha 410083, Hunan, China

² School of Civil Engineering, Southeast University, Nanjing 211189, China

cracks due to transversal tensile stress and (2) failure either by buckling of a few slender pillars formed between cracks or by global deformation and simultaneous instability of a series of micro-pillars along inclined “sliding” planes. Qiu et al. (2014) studied the evolution and formation mechanism of slabbing and rockbursts in deep tunnels by true-triaxial loading–unloading tests and discussed the important role of severe rockburst induced by slabbing failure. Du et al. (2016) conducted true-triaxial unloading tests, and the results indicated that occurrence of slabbing and rockburst are closely related to the rock type and stress path. Li et al. (2017, 2018a) investigated the failure properties influenced by specimen height-to-width ratios and intermediate principal stress in true triaxial unloading compression test and revealed that the rock unloading may induce slabbing. These studies are useful for investigating spalling failure.

Furthermore, spalling failure of tunnel or cavern surrounding rock in underground engineering is affected by the stress state and the tunnel cross section shape. Some scholars have carried out a series of experimental studies and numerical simulations on spalling failure (Gay 1976; Cheon et al. 2006, 2011; Sagong et al. 2011; Hidalgo and Nordlund 2012; He et al. 2012, 2014; Zhou et al. 2016; Gong et al. 2018a, 2019a). Gay (1976) conducted uniaxial and biaxial compression tests using blocks of quartzite and sandstone containing holes of circular or rectangular cross sections. They observed that spalling occurred at the ends of the long axis of the hole and extension cracks formed in the center. Sagong et al. (2011) analyzed the rock fracture and joint sliding behaviors of jointed rock masses of a circular tunnel according to the biaxial compression tests and numerical simulation. Cheon et al. (2006, 2011) conducted true-triaxial physical model experiments on a cement mortar to simulate the spalling failure of circular tunnel sidewall and clearly observed a V-shaped notch by computed tomography (CT). Hidalgo and Nordlund (2012) presented a comparison of laboratory tests and numerical modeling results to evaluate spalling failure in hard rock and further demonstrated that the onset of cracking calculated from laboratory tests can be related to the in situ crack initiation strain. He et al. (2012, 2014) conducted true-triaxial tests on $110 \times 110 \times 110 \text{ mm}^3$ sandstone specimens with a $\Phi 50 \text{ mm}$ cylindrical hole, proposed a new classification of rockburst based on the rockburst testing devices and characteristics of the stress states. Gong et al. (2018a, 2019a) conducted spalling and rockburst simulation tests on Red Sandstone and granite cubic specimens with a circular hole under 3D high-stress conditions. They observed the rockburst processes and development of a symmetrical V-shaped notch and studied the mechanism of rockburst induced by spalling. Zhou et al. (2016) performed simulation tests on rock-like specimens of circular caverns with different diameters and D-shaped caverns with different sizes. The curvature radius of the excavation cross

section influences the mechanism of the spalling failure of surrounding rock in two aspects: scale effect and structure effect. Numerical simulation results were used to analyze and verify the effect of the curvature radius of the excavation cross section on the spalling failure. The above studies mainly focus on simulation tests of the circular cross section tunnel. There are few reports on the investigation of rock materials with D-shaped holes. In deep underground engineering, the actual roadway or tunnel is in a 3D high-stress state. From the perspective of 3D stress state, the failure process and characteristics of D-shaped cross section tunnel are closer to the actual situation at large depth. Therefore, it is motivated to conduct experimental research on the failure process and mechanism of D-shaped cross section tunnel under true-triaxial high-stress conditions.

In this study, true-triaxial loading tests are conducted using a true-triaxial testing machine on 100 mm cubic granite specimens containing a through D-shaped hole under different initial stress states. During the tests, the spalling failure process of hole sidewall is monitored and recorded in real time by a wireless microcamera. The experimental results are analyzed in detail and the influence of the stress state on the spalling failure severity of the D-shaped hole sidewall is investigated.

2 Experimental Procedures

2.1 Specimen Preparation

The experimental material selected for this study was fine-grained granite from Changtai County, Zhangzhou City, Fujian Province, China. The naked-eye observation photograph of the fine-grained granite material is shown in Fig. 1a. To determine the mineral composition and structure of the rock, thin section of a rock was studied with a petrographic microscope under single and orthogonal polarized light, as shown in Fig. 1b and c (Gong et al. 2019b). The mineral composition of the rock is approximately 49% quartz, 43% plagioclase, 4% biotite, 3% hornblende, and 1% opaque minerals. The rock is classified as fine-grained massive-structure granite.

To simulate the failure process of the rock surrounding D-shaped tunnel, the fine-grained granite material was processed into four 100 mm cubic specimens with a through D-shaped hole, with a sidewall height 25 mm, width 50 mm, and arch height 25 mm, as shown in Fig. 2. The machining precision strictly followed the International Society for Rock Mechanics (ISRM) standards. The recommended standard tolerance is 0.0175 mm for the given dimensions of $100 \text{ mm} \times 100 \text{ mm} \times 100 \text{ mm}$, and the perpendicularity tolerance is 0.025 mm for each side as a datum plane (Feng et al. 2019). The basic physical and mechanical parameters

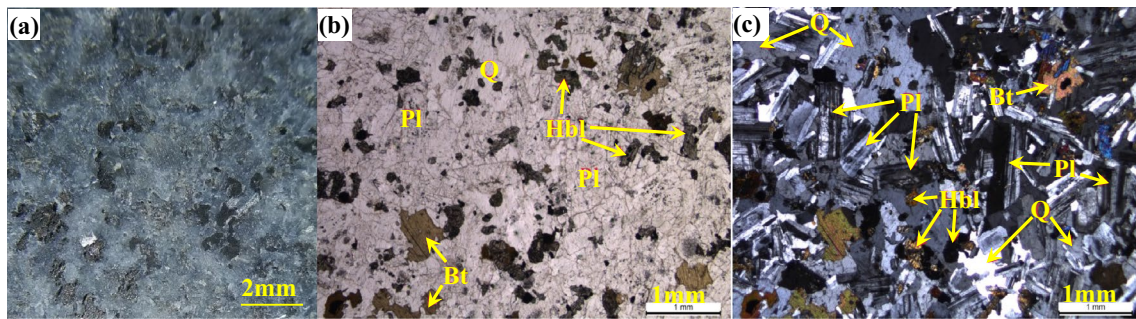


Fig. 1 Granite material: **a** naked-eye observation, **b** single polarized light, and **c** orthogonal polarized light (the letters Q, Pl, Bt, and Hbl represent quartz, plagioclase, biotite, and hornblende, respectively) (Gong et al. 2019b)

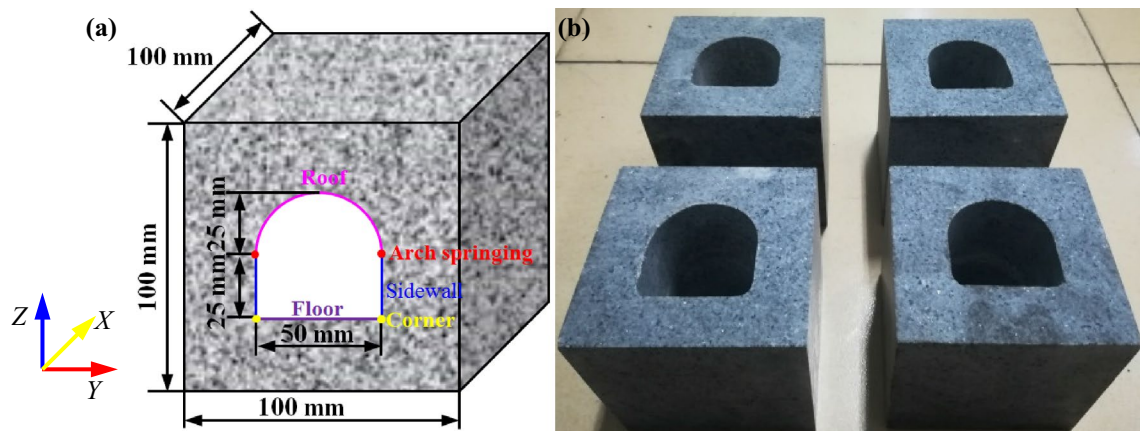


Fig. 2 Cubic granite specimens: **a** schematic illustration of the specimen size, **b** photograph of granite specimens

Table 1 Basic physical and mechanical parameters of the fine-grained granite material

Density (g·cm ⁻³)	P-wave velocity (km/s)	Uniaxial compression strength (MPa)	Brazilian splitting strength (MPa)	Young's modulus (GPa)	Rockburst proneness
2.766	4.9	261.6	6.5	57.9	Strong

are listed in Table 1. The fine-grained granite material has strong rockburst proneness according to the residual elastic energy index (Gong et al. 2018b) and the peak strain energy storage index (Gong et al. 2019c).

2.2 True-Triaxial Testing Machine

The tests were carried out using a true-triaxial testing machine, as shown in Fig. 3a and b. Detailed introduction of the experimental equipment is provided in Gong et al. (2018a, 2019a) and Li et al. (2018b). The combination of the microcamera and the X-direction loading block is shown

in Fig. 3c. The failure process of the D-shaped hole sidewall was monitored in real time using a XM-JPG1-4S micro-camera (Fig. 3d). The camera was mounted in a Φ50 mm cylindrical circular hole in the X-direction loading block.

2.3 Loading Scheme

The in situ stress state can be estimated according to Brown and Hoek (1978) and Stephansson et al. (1986). To simulate the spalling failure characteristics of D-shaped tunnel sidewall at depth of 1000 m, the values of the in situ stresses are used to apply at the specimen faces as an initial stress state. The results are $\sigma_z = \sigma_v = 27$ MPa, $\sigma_{hmax} = 51$ MPa, $\sigma_{hmin} = 34$ MPa, and the four combinations of the horizontal stresses σ_{hmax} and σ_{hmin} are shown in Fig. 4. The stress values given in the paper from now on are referred to as nominal stress values applied on the specimen faces.

Figure 5 shows the loading path of the true-triaxial test. The cubic granite specimen was installed in the loading box, and the loads in three (X, Y, and Z) directions were increased to the initial stress state by load control at the loading rate of 1000 N/s. The loading method in the X-direction was

Fig. 3 Experimental equipment: **a** true-triaxial testing machine, **b** cubic specimen loading chamber, **c** combination of microcamera and X-direction loading block, and **d** wireless microcamera

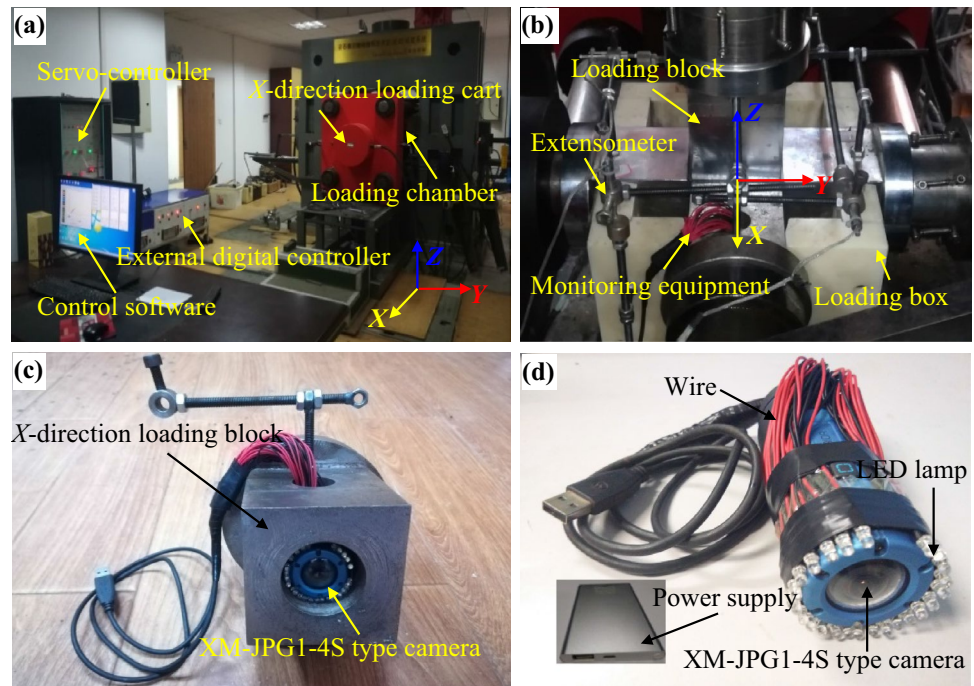
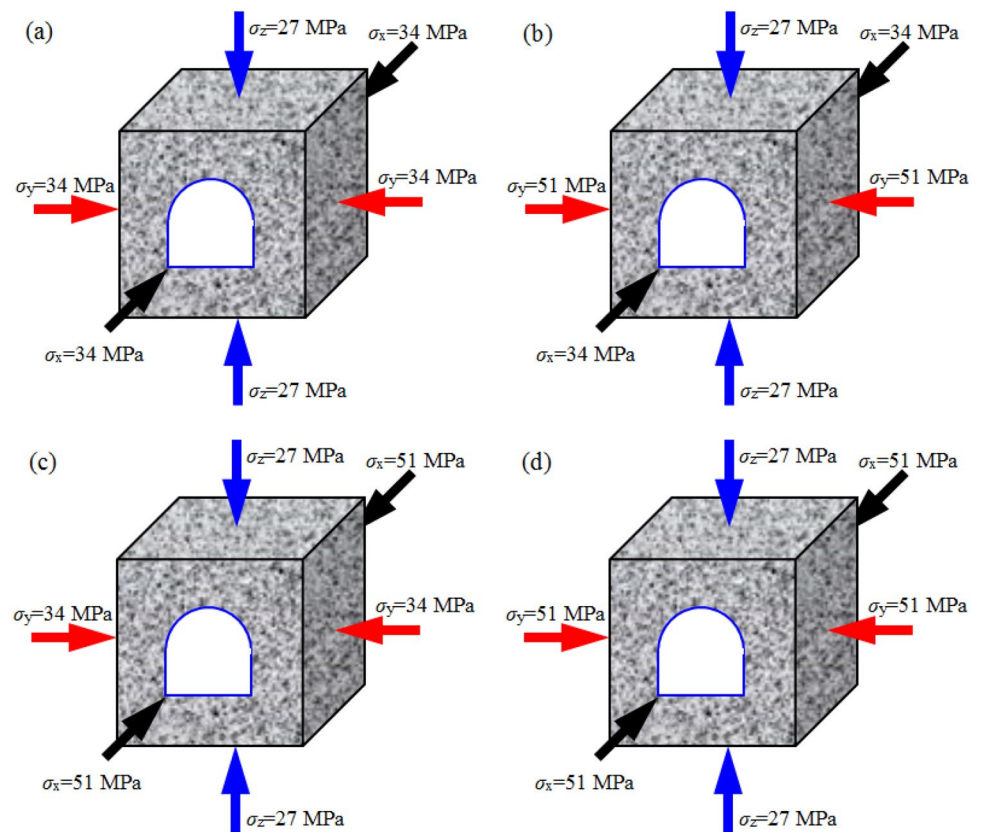


Fig. 4 3D initial stress diagrams under four stress conditions: **a** HZ-34-34, **b** HZ-34-51, **c** HZ-51-34, and **d** HZ-51-51



changed to displacement control and the displacement in the X-direction is kept constant (simulating generalized plane-strain). Continue to apply load control in the Y-direction and

keep Y-direction stress constant. The load in the Z-direction continued to increase at the same loading rate up to 68.0 MPa (The process of stress adjustment is simulated by

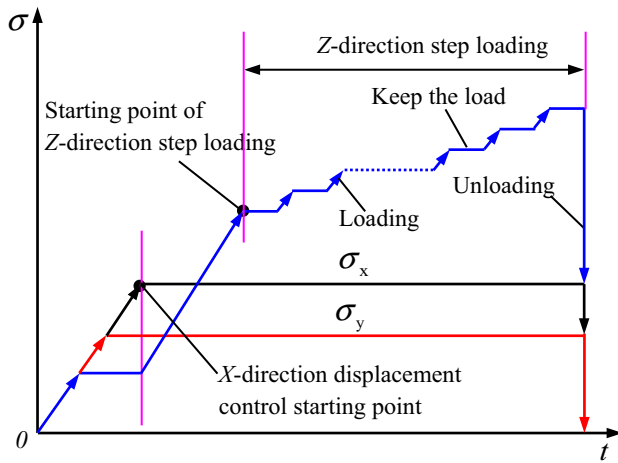


Fig. 5 Schematic of stress path (Gong et al. 2018a)

increasing the vertical stress). The load was then increased stepwise in 2.0 MPa steps and with a hold time of approximately 1 min in between to ensure that the specimen does not suddenly instability. When serious spalling failure occurred on both sidewalls of the D-shaped hole, the load

was maintained for a period of time, and then the loads in three directions were unloaded to 0 MPa using the displacement rate of 20 mm/min.

3 Experimental Results

3.1 Stress Versus Time

The actual stress–time curves of the three directions under four 3D stress conditions are shown in Fig. 6. From Fig. 6, the stress in the X-direction produced slight fluctuation due to the change of loading method. The Z-direction stress under the four stress conditions were loaded to 166.0 MPa(HZ-34-34), 170.0 MPa(HZ-34-51), 162.0 MPa(HZ-51-34), and 172.0 MPa(HZ-51-51), which were divided into 50, 52, 48, and 53 steps, respectively, starting from 68 MPa.

3.2 Spalling Failure Process of the Hole Sidewall

To observe and record the failure process of the hole sidewall in real time, a wireless microcamera was used. The

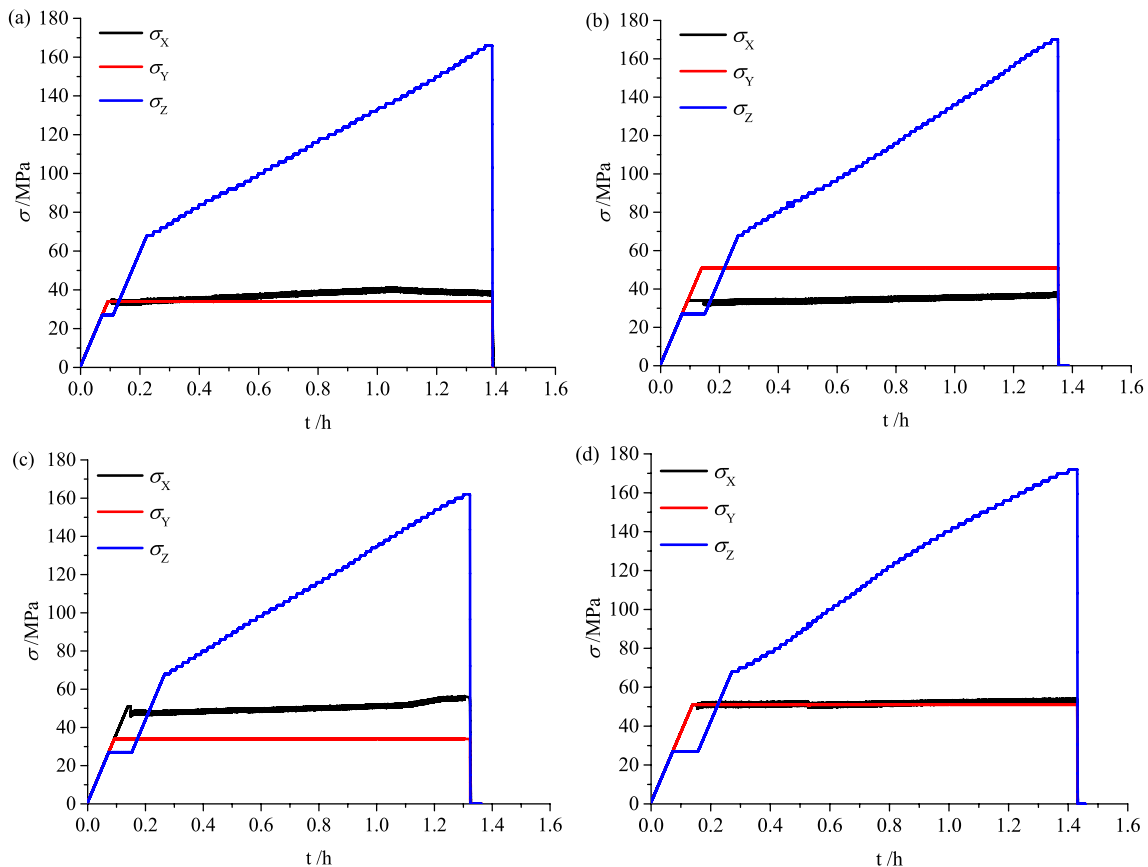


Fig. 6 Stress-time curves: a HZ-34-34, b HZ-34-51, c HZ-51-34, and d HZ-51-51

spalling failure processes of the hole sidewall under four 3D stress conditions are shown in Figs. 7, 8, 9, and 10. The specimen HZ-34-34 is taken as an example to describe the failure process of the hole sidewall in detail (see Fig. 7). In the process of loading to the initial stress levels in X-, Y-, and Z-directions, there is no failure on the sidewalls of the hole. The vertical stress was then increased in steps and observations made are described below. Step 13 (92.0 MPa, 1797.64 s, Fig. 7a): Fine particle ejection occurred at the right corner, and the particles ejected upward obliquely to the free surface. Step 21 (108.0 MPa, 2527.84 s, Fig. 7b): The right sidewall produced a fine rock fragment, but it remained vertical and did not dump. During the continuous loading process, slight fine particle ejection also appeared on the left and right sidewalls. Step 22 (110.0 MPa, 2603.28 s, Fig. 7c): A new crack occurred on the right sidewall, accompanied by a slight splitting sound. The crack developed from the corner along the sidewall to the arch springing (the arch springing is the junction of the sidewall and the roof). The development direction is approximately parallel to the vertical direction. With increasing vertical stress, the newly produced crack in Fig. 7c gradually expanded to form spalling structure and the rock slab gradually buckled from the corner to the state in Step 28 (122.0 MPa, 3113.48 s, Fig. 7d), in which a small angle is formed between the rock slab and the vertical sidewall. From Fig. 7d, new cracks were produced in the process of rock slab buckling. Step

28 (122.2 MPa, 3171.08 s, Fig. 7e): A new crack occurred at the right sidewall accompanied by fine particle ejection at the location of crack initiation, which indicates that the high energy accumulated and stored in the sidewall of the hole mainly converts into the required fracture energy for crack initiation and the kinetic energy of particle ejection. Step 30 (126.0 MPa, 3329.88 s, Fig. 7f): The right sidewall produced the first spalling rock slab, but the rock slab was still in the upright state and there was no dumping. Step 33 (131.7 MPa, 3518.16 s, Fig. 7g): A new crack was generated at the left sidewall. Step 33 (132.0 MPa, 3556.44 s, Fig. 7h): The cracks in Fig. 7d and g gradually expanded and penetrated, extending along the sidewall to the arch springing, and a new crack was produced near the penetrated large crack. With increasing σ_z , the cracks on both sidewalls in Fig. 7i–k expanded, and the rock slabs gradually buckled from the corner forming spalling structure. In Fig. 7k, the spalling failure developed along the lateral direction to the depth of the sidewalls, and the crack propagated in the inner layer and the rock slab gradually buckled to contact the exfoliated rock slab of the outer layer and produced interacting force, which led to the dumping of the outer rock slab. Step 37 (140.0 MPa, 3935.52 s, Fig. 7l): The outermost rock slab of the left sidewall flaked, while multiple rock slabs of right sidewall from the outer to inner layer flaked simultaneously. Prior to this, the left and right sidewalls had only produced independent rock slab spalling. When the vertical stress is

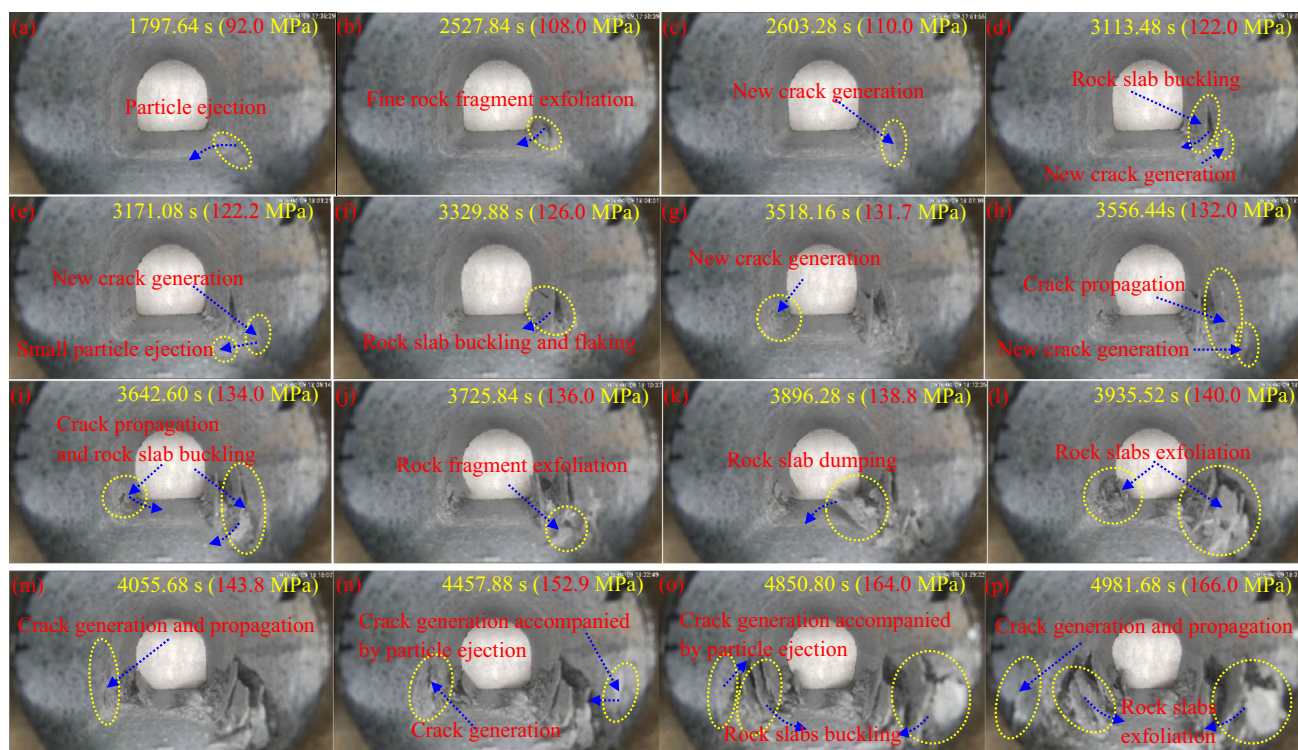


Fig. 7 Spalling failure process of specimen HZ-34-34

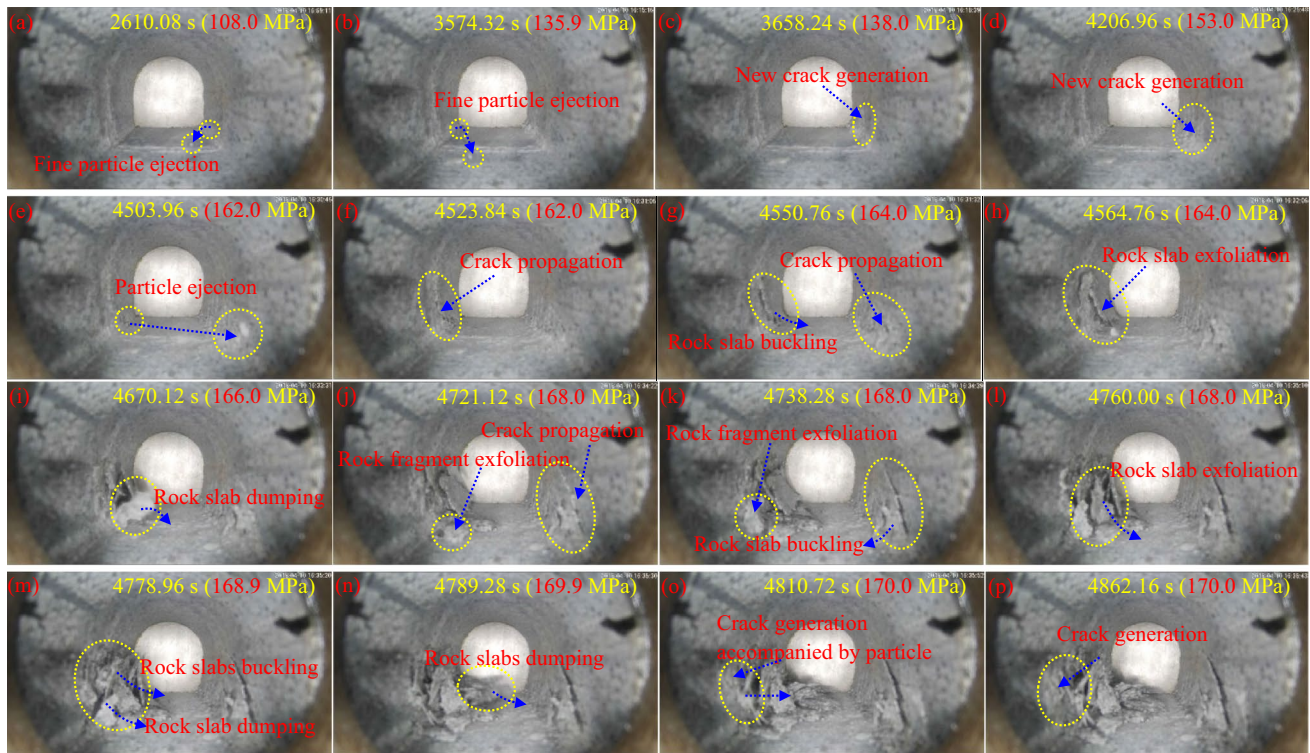


Fig. 8 Spalling failure process of specimen HZ-34-51

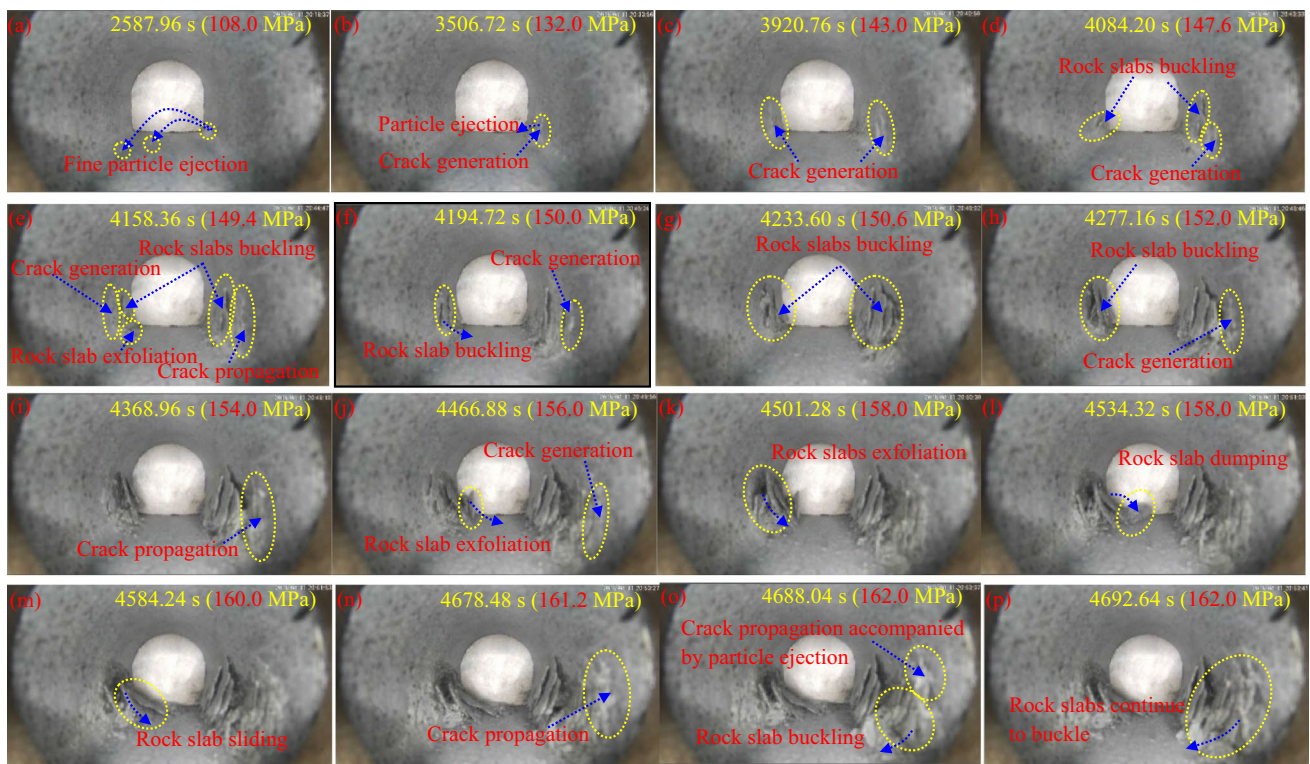


Fig. 9 Spalling failure process of specimen HZ-51-34

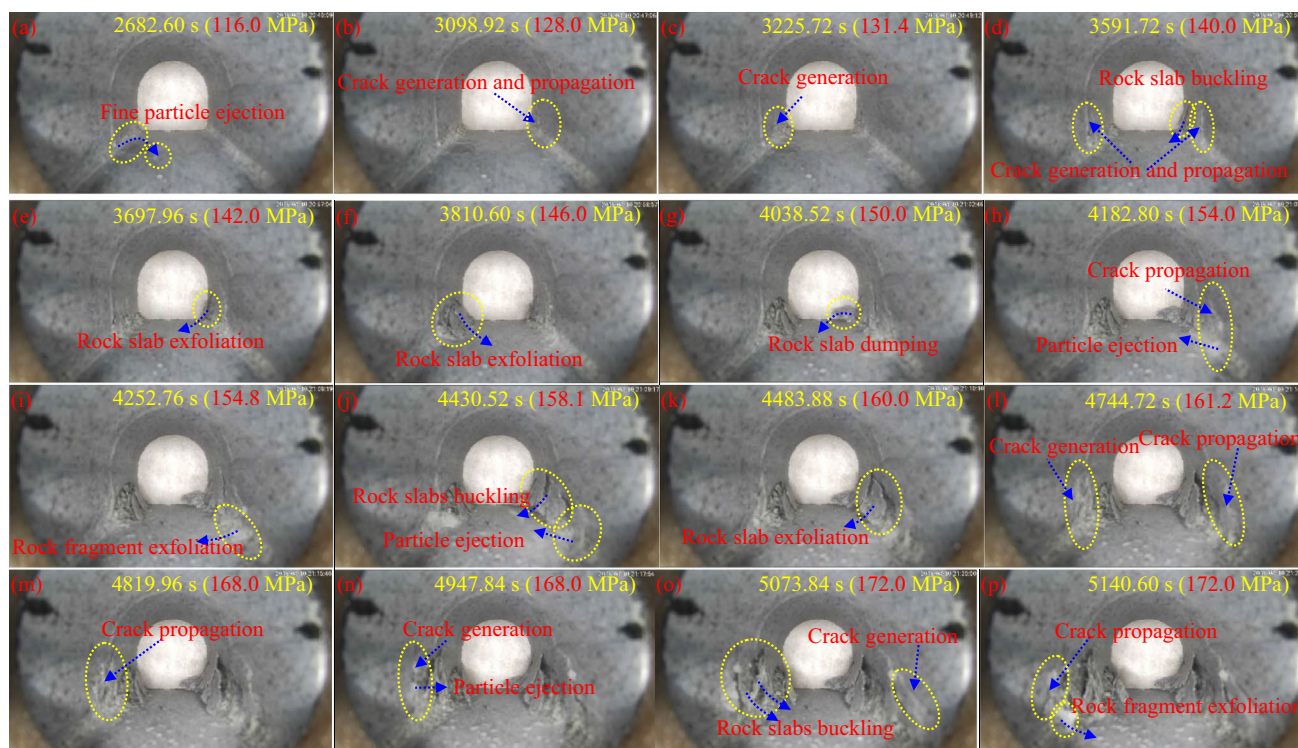


Fig. 10 Spalling failure process of specimen HZ-51-51

high, a large amount of energy is accumulated in the hole sidewall, which leads to the spalling failure of multi-layer rock slabs along the lateral direction to the deep surrounding rock. Step 39 (143.8 MPa, 4055.68 s, Fig. 7m): A new crack was produced on the left sidewall, and it expanded from the corner to the arch springing. Step 44 (152.9 MPa, 4457.88 s, Fig. 7n): It can be observed that a new vertical and visible crack was produced on the right sidewall, which was accompanied by a small amount of particle ejection. In contrast to Fig. 7c–d and n, under the low vertical stress condition, and there was no ejection of particles when crack occurred, which indicates that the energy accumulated in the sidewall was small at the time. During loading to step 49 (164.0 MPa, 4850.80 s, Fig. 7o), the cracks on the left and right sidewalls gradually expanded, the rock slabs gradually buckled to form spalling structure, and the middle and lower parts of the rock slabs were separated from the sidewall. Only the upper part of the rock slab near the arch springing was connected with the sidewall. This shows that the spalling failure process of the sidewall is relatively slow and the intensity is relatively low. In Fig. 7o, a new crack was generated on the left sidewall near the camera, accompanied by a small amount of particle ejection and a crisp splitting sound. This crack gradually extended to the edge of the specimen during the increase in the vertical stress. In addition, the buckling rock slabs on both sidewalls flaked and slipped from the corner to the free surface, and the upper part was leaning on the

sidewall. Until step 50 (166.0 MPa, 4981.68 s, Fig. 7p): The spalling failure of both sidewalls ran through the whole specimen along the axis of the hole, and then the stresses in three directions were unloaded to 0 MPa after maintaining about 60 s. According to the failure process of specimen HZ-34-34 on both sidewalls, it can be observed that the spalling failure can occur at the stage of stress loading or during stress constant loading. The spalling failure is relatively slow, and it is a progressive failure process.

The spalling failure processes of specimens HZ-34-51, HZ-51-34, and HZ-51-51 are similar to those of specimen HZ-34-34, as shown in Figs. 8, 9, and 10, respectively. In summary, in the spalling failure process on both sidewalls, fine particle ejection was generated at the corner. With increasing vertical stress, a crack was generated and propagated from the corner to the arch springing, which is approximately parallel to the sidewall. Then, the rock slab gradually buckled and finally flaked. Because the spalling failure process of the sidewall is relatively slow and takes a long time, during this process, particle ejection, crack generation, and crack propagation occurred in other positions of both sidewalls. Furthermore, the spalling failure gradually developed into the depth of both sidewalls and penetrated the entire specimen along the hole axial direction, and symmetrical V-shaped notches were formed on the left and right sidewalls of the hole.

3.3 Failure Characteristics of the Hole Sidewall

The overall and local damage of the fine-grained granite specimens after the experiment are shown in Fig. 11. To see the V-shaped notches formed on both sidewalls of the D-shaped hole more clearly, the photographing direction of the photographs in Fig. 11 is opposite to that of the video screenshot in Figs. 7, 8, 9, and 10. The specimens HZ-34-34, HZ-34-51, HZ-51-34, and HZ-51-51 are not unstable, spalling failure occurred on both sidewalls of the hole, and the symmetrical V-shaped failure zone is formed on both sidewalls of the hole. From Fig. 11, the rock slab spalling occurred on the outer sidewall of the failure zone. The cracks in the inner layer of the failure zone can be clearly observed; they are approximately parallel to the sidewall (the vertical direction). Therefore, the spalling failure is characterized by tensile failure. The sidewalls of specimens HZ-34-34 (Fig. 11a), HZ-34-51 (Fig. 11b), HZ-51-34 (Fig. 11c), and HZ-51-51 (Fig. 11d) formed V-shaped failure zones. From Fig. 11a, c, and d, the rock slabs produced leaned on the sidewall of the hole. In Fig. 11b, the rock slabs on the right sidewall fell to the floor and the rock slab on the left side wall buckled at the floor but the upper part did not separate from the sidewall. In summary, the rock slabs formed by the spalling failure of the sidewall mainly show buckling at the lower part. When the upper part is completely separated from the sidewall, the rock slabs slip gradually toward the free surface. Therefore, the spalling failure of the hole sidewall is a progressive process.

Figure 12 shows the shape of the failure zones on both sidewalls after the slabs were generated by the sidewalls. It can be seen from Fig. 12 that the shape of the final failure zone under different stress states is similar for all specimens and forms a V-shape. From shallow to deep, the failure zone gradually evolves into a V-shaped notch. The V-shaped notch with deep middle and shallow sides basically penetrates the specimen along the axis direction and is formed on both sidewalls. The V-shaped notch is located between the corner and the arch springing, and the V-shaped notches on left and right sidewalls are symmetrical with respect to the vertical centerline. The characteristics of the rock slabs produced on the hole sidewall, as shown in Fig. 13, are further investigated. From the photographs of the rock slabs in the X - Y plane in Fig. 13a, the two typical rock slabs were divided into three layers by two cracks in the middle. From Fig. 13b, the rock slabs on the left in the X - Y plane were divided into five layers by four cracks, and the adjacent rock slab was divided into two layers by one crack. The two slabs in Fig. 13c were divided into three layers by two cracks. Similarly, the two slabs in Fig. 13d were divided into two layers by one crack. These results show that the slabs exhibit a layer splitting phenomenon. Although different rock slabs are

divided into multiple layers by cracks, each layer of the slabs is not completely separated. The rock slabs are thick in the middle and thin at the edge, and the surface of the rock slabs are smooth. There is no rock powder produced on the surface of the rock slabs, as shown in the partial enlarged view of the rock slabs in Fig. 13. This further shows that the spalling failure of both sidewalls exhibits tensile failure characteristics.

4 Discussions

4.1 Comparison of the Experiments and Engineering

The spalling failure of deep tunnel or cavern surrounding rock in actual underground engineering is shown in Fig. 14. Figure 14a shows the spalling failure of a D-shaped tunnel at a depth of 1000 m in Linglong gold mine, approximately parallel to the right sidewall. Rock spalling failures of the deep tunnel in Jinping Underground Laboratory, China, are shown in Fig. 14b and c. The cracks in the surrounding rock of the tunnel are parallel to the maximum principal stress, which is characterized by tensile failure (Bobet and Einstein 1998; Haimson 2007; Si and Gong 2020; Qiu et al. 2020). Comparing Fig. 11 with Fig. 14, the failure mode of the in situ tunnel sidewall during the test is consistent with observations from deep tunnels in underground engineering, i.e., the sidewall of the D-shaped tunnel produced spalling failure, and it has tensile failure characteristics. This shows the rationality of the simulation tests.

According to the test results under different stress conditions, it has been found that the locations of initial failure were on the corner of the D-shaped hole during the step loading of vertical stress, and the failure location is not affected by the horizontal stress state. This indicates that the corner of the D-shaped hole has a high stress concentration coefficient and is the most likely location of failure. When the D-shaped tunnel is adopted in underground engineering, the corner of the D-shaped hole should be strengthened and supported to increase the bearing capacity and reduce the failure risk of the surrounding rock. For example, under the original support design scheme of the deep D-shaped roadway in Maluping Mine, Guizhou Province, China (see Fig. 15a), failure occurred at the corner of the roadway (see Fig. 15b). Compared with the original support design scheme, the newly designed support plan (see Fig. 15c) added energy absorption anchors at the corner, which played a better supporting role and limited the failure of the corner. Therefore, supporting the corner of D-shaped roadway has an important role in maintaining the stability of the surrounding rock.

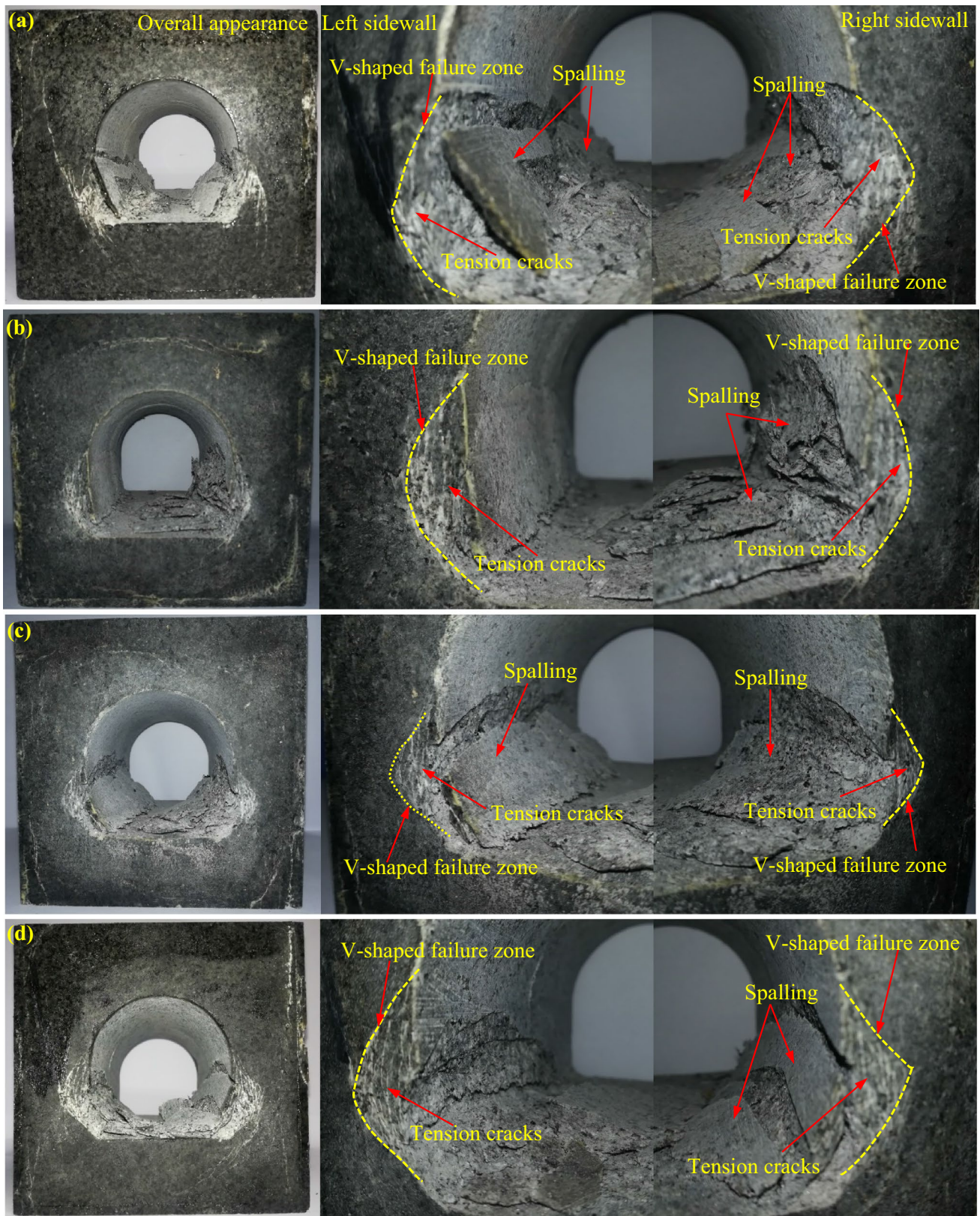


Fig. 11 Failure of the overall specimen and the left and right sidewalls of the tunnel: **a** HZ-34-34, **b** HZ-34-51, **c** HZ-51-34, and **d** HZ-51-51

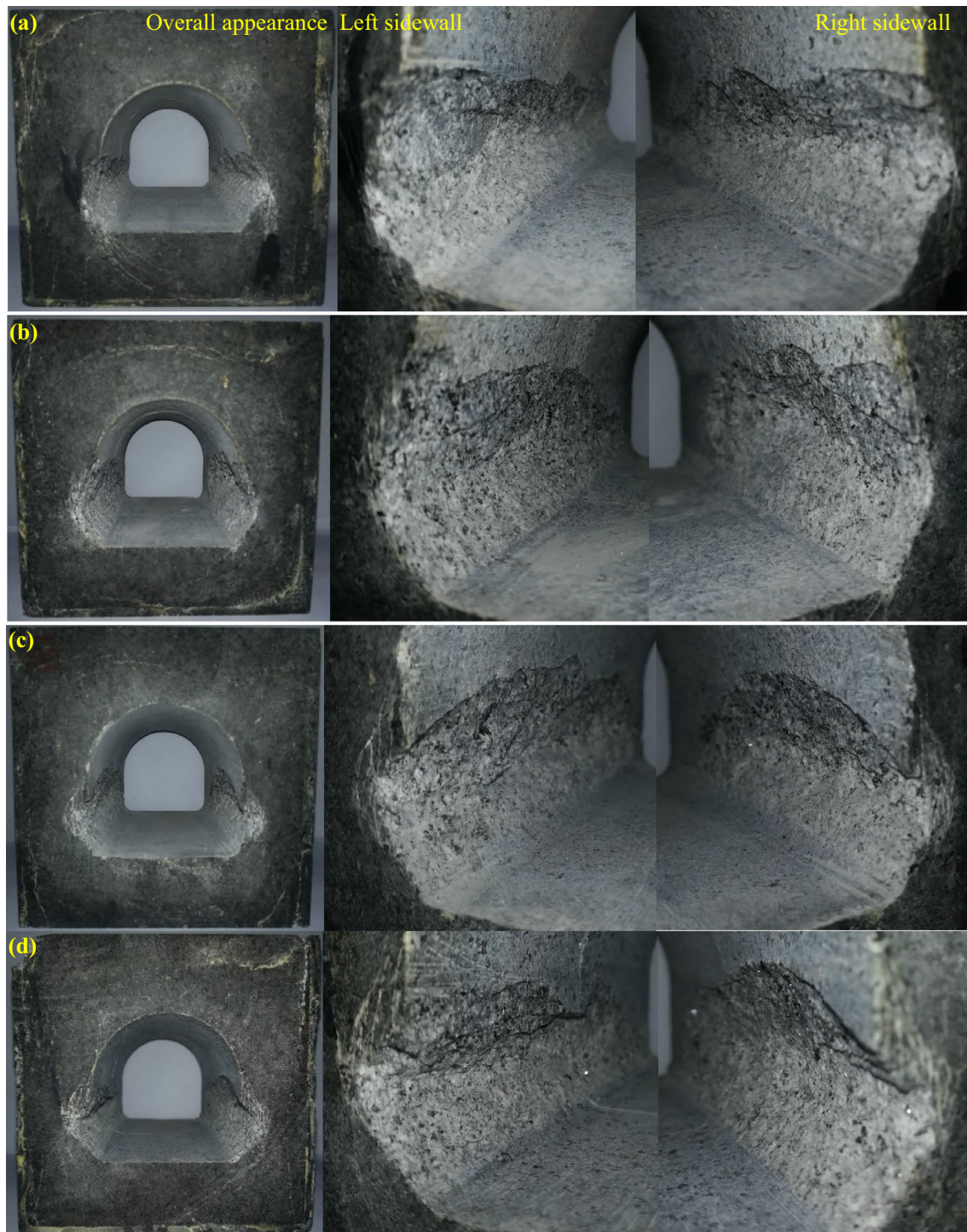


Fig. 12 Morphological characteristics of the failure zone of sidewalls in a D-shaped hole: **a** HZ-34-34, **b** HZ-34-51, **c** HZ-51-34, and **d** HZ-51-51

4.2 Evolution Process of Spalling Failure

In the test, after the stresses in the X -, Y -, and Z -directions were loaded to the set stress state, the vertical stress was increased after maintaining for a period of time. During

steploding of vertical stress (simulating the stress adjustment in actual engineering), the failure of the D-shaped hole sidewall occurred. Rockburst statistics from on-site failures show that most rockbursts occur during the later stress adjustment process. Jiang et al. (2010) reported the

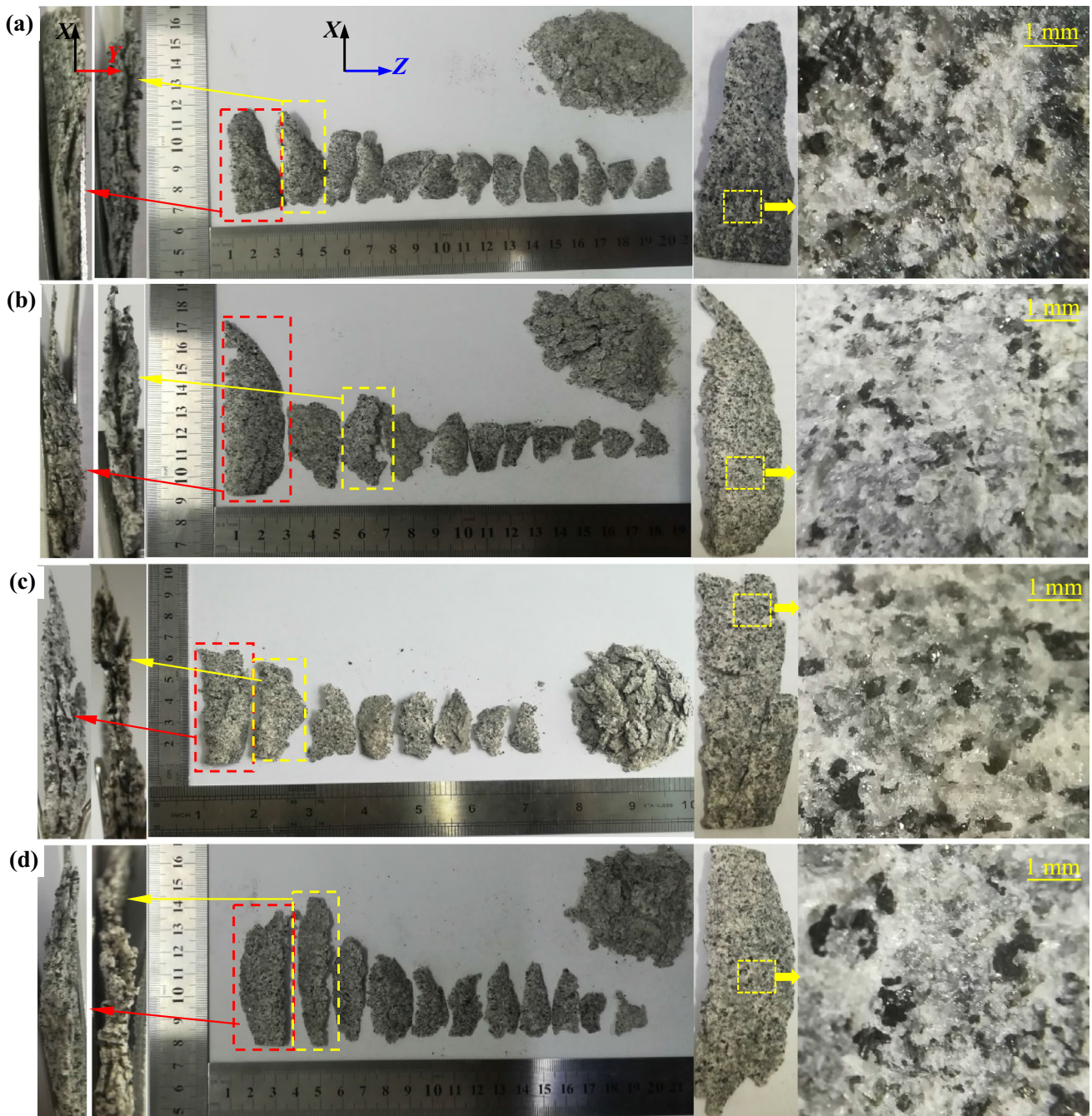


Fig. 13 Rock slabs caused by spalling failure of sidewall and their local enlargement images: **a** HZ-34-34, **b** HZ-34-51, **c** HZ-51-34, and **d** HZ-51-51

delay between excavation and rockburst of Jinping II Hydro-power Station, as shown in Fig. 16. The results show that most rockbursts happen within a few hours of the excavation ended, and the rest typically within 20 h. Rockbursts have occurred a long time after the excavation unloading process, when the surrounding rock was in the process of slow stress adjustment. Therefore, the surrounding rock undergoes spalling or rockburst after a long period of stress

adjustment. In the tests, the times from the initial in situ stress to the initial failure of the hole sidewall under the four stress conditions are shown in Table 2. From Table 2, T_d is 1463.92 s (HZ-34-34), 2107.52 s (HZ-34-51), 2077.91 s (HZ-51-34), and 2179.32 s (HZ-51-51), respectively. This indicates that the spalling failure of the hole sidewall has undergone after a long time of stress adjustment. In Table 2, when σ_x is 34.0 MPa or 51.0 MPa and σ_y increases from 34.0

Fig. 14 Photograph of spalling failure of a D-shaped tunnel in underground engineering: **a** spalling failure of the D-shaped tunnel at a depth of 1000 m in Linglong gold mine, China, **b-c** rock spalling failure in the deep tunnels of the China Jinping Underground Laboratory (Feng et al. 2018)

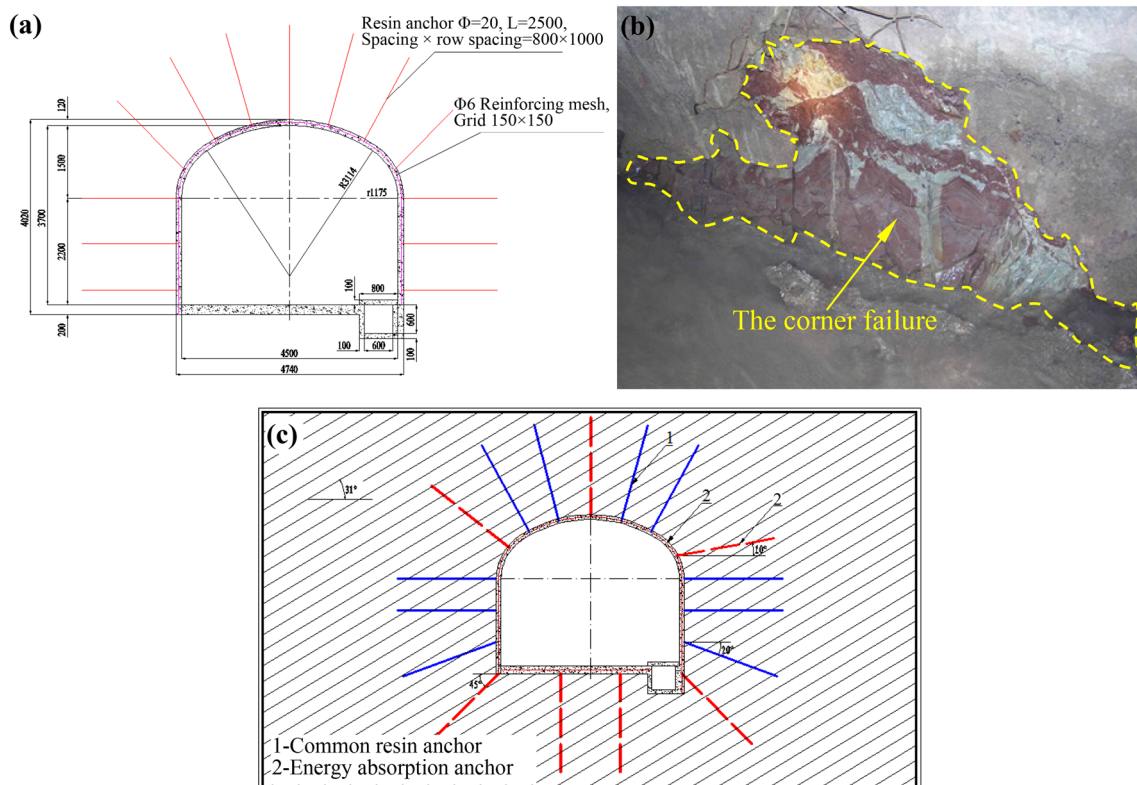
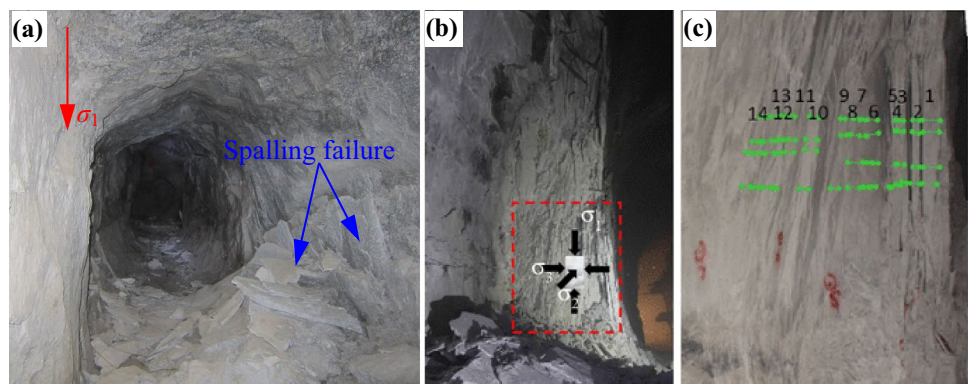


Fig. 15 Comparison of support scheme for deep roadway design in Maluping Mine: **a** original support design plan, **b** the corner failure, and **c** newly designed support plan

to 51.0 MPa, the initial failure stress of the D-shaped hole sidewall increases. The smaller σ_y is, the more easily failure of the D-shaped hole sidewall occurs. Therefore, increasing σ_y can reduce the possibility of surrounding rock failure when σ_x is constant.

By observing the failure process of the D-shaped hole sidewalls under different 3D stress conditions, the spalling failure process is determined to proceed as shown in Fig. 17. The process can be divided into four periods over increasing vertical stress σ_z (σ_1): (1) calm period, (2) fine particle ejection period, (3) crack generation and propagation period, and (4) rock slab gradually buckling and spalling period.

The characteristics of these four periods are explained in detail as follows.

(1) Calm period: There is no damage on the hole sidewall, and strain energy is stored and accumulated. In addition, micro-cracks are initiated and propagated in the surrounding rock, and this lays a foundation for spalling failure. The schematic of this period is shown in Fig. 17a.

(2) Fine particle ejection period: With increasing vertical stress, the accumulated energy in the surrounding rock gradually increases, until the vertical stress exceeds the bearing capacity of the surrounding rock and causes failure. This period is the initial failure period of the sidewall. Fine

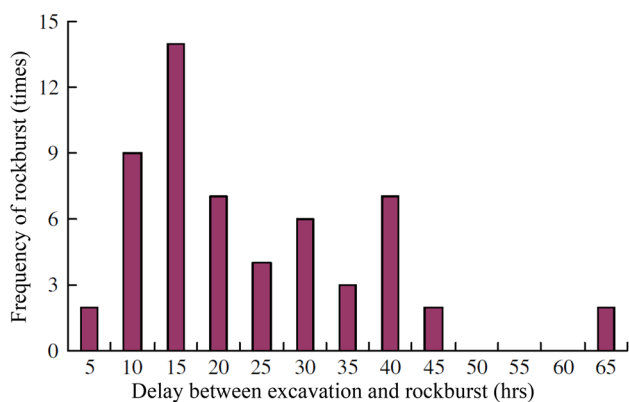


Fig. 16 Diagram of rockburst time character (Jiang et al. 2010)

particle ejection occurs at the corner (see Fig. 17b), mainly because the corner is a high-stress concentration zone, which is prone to failure. With increasing vertical stress, the corner produces multiple particle ejections that develop along the axis direction of the hole.

(3) Crack generation and propagation period: Cracks are generated on the D-shaped hole sidewall and propagated from the corner to the arch springing with increasing vertical stress, and the crack propagation direction is approximately parallel to the sidewall, as shown in Fig. 17c. In addition, when the vertical stress is high, the high elastic strain energy accumulates in the hole sidewall; therefore, cracks propagate on both sidewalls accompanied by particle ejection, as shown in Figs. 7o, 8o, 9o, and 10n.

(4) Rock slab gradually buckling and spalling period: After the cracks on the sidewalls extend to the arch springing, the rock slab gradually expands from the corner to the free surface under the action of the vertical stress. Finally, the rock slab flakes from the hole sidewall. The schematic of this period is shown in Fig. 17d. It can be seen from Figs. 7, 8, 9, and 10 that rock slab buckling is a slow process. Therefore, this period takes a long time. During this period, particle ejection, crack generation, and propagation continue to occur at other positions of both sidewalls.

During the spalling failure of the D-shaped hole sidewalls, two or more of the above four periods occurred

simultaneously in different positions of the sidewall under the condition of high vertical stress, i.e., crack generation and propagation occurred at one location, at the same time rock slab gradually buckling and spalling occurred at another location, as shown in Fig. 7e, h, i, o, and p. Finally, the spalling failure gradually developed to the depth and formed symmetrical V-shaped failure zones on both sidewalls. Different periods occurred simultaneously in different positions of the sidewall, this shows that the failures of the D-shaped hole sidewalls is characterized by spatial distribution.

4.3 Influence of Stress State on Spalling Failure

The failure of deep rock is closely related to the stress state, and the severity of the surrounding rock failure of a tunnel or cavern is affected by the stress state. Gong et al. (2018a, 2019a) investigated how the rockburst severity of a circular cavern is affected by the stress state. To study the influence of the stress state on the severity of the spalling failure, the depth and location of the failure zone, four simulation experiments under different initial stress states were carried out.

The depth and location of the failure zone on both sidewalls under different stress conditions were measured, and the measurement results are summarized in Table 3. From Table 3, when $\sigma_x = 34.0$ MPa and σ_y is increased from 34.0 to 51.0 MPa, the average depth of the failure zone of the left and right sidewalls is reduced from 7.91 to 6.49 mm, a decrease of 1.42 mm. Similarly, when σ_x is 51 MPa, the average depth is reduced from 7.76 to 7.40 mm, a decrease of 0.36 mm. It can be concluded that when the horizontal axial stress is constant, the higher the lateral stress, the shallower the failure zone on both sidewalls of the D-shaped tunnel. When the horizontal axial stress is low and the lateral stress increases by 17.0 MPa from 34.0 to 51.0 MPa, the depth of the failure zone decreases more obviously, i.e., the decreased value of $\sigma_x = 34$ MPa is higher than that of $\sigma_x = 51.0$ MPa (1.42 mm > 0.36 mm). Comparing the positions of the tips of the V-shaped notches under different stress conditions, when the maximum principal stress is the vertical direction, 10.21 mm is the minimum data; 12.18 mm is the maximum data, as shown in Table 3. Therefore, the range of distance between the tip of V-shaped notch and the floor of D-shaped

Table 2 Difference time between initial failure stress and initial vertical in situ stress

Specimen no.	σ_x (MPa)	σ_y (MPa)	σ_{vi} (MPa)	T_1 (s)	σ_{zi} (MPa)	T_2 (s)	T_d (s)
HZ-34-34	34.0	34.0	27.0	333.72	92.0	1797.64	1463.92
HZ-34-51	34.0	51.0	27.0	502.56	108.0	2610.08	2107.52
HZ-51-34	51.0	34.0	27.0	510.05	108.0	2587.96	2077.91
HZ-51-51	51.0	51.0	27.0	503.28	116.0	2682.60	2179.32

Note: σ_{vi} is initial vertical in situ stress; T_1 is the time taken to load to the initial in situ stress; σ_{zi} is initial failure stress in the Z-direction; T_2 is the time taken to load to the initial failure stress; T_d is the difference time between T_2 and T_1

Fig. 17 Schematic of the evolution of spalling failure in a D-shaped tunnel with increasing vertical stress σ_z (σ_1): **a** calm period, **b** fine particle ejection period, **c** crack generation and propagation period, and **d** rock slab gradually buckling and exfoliation period

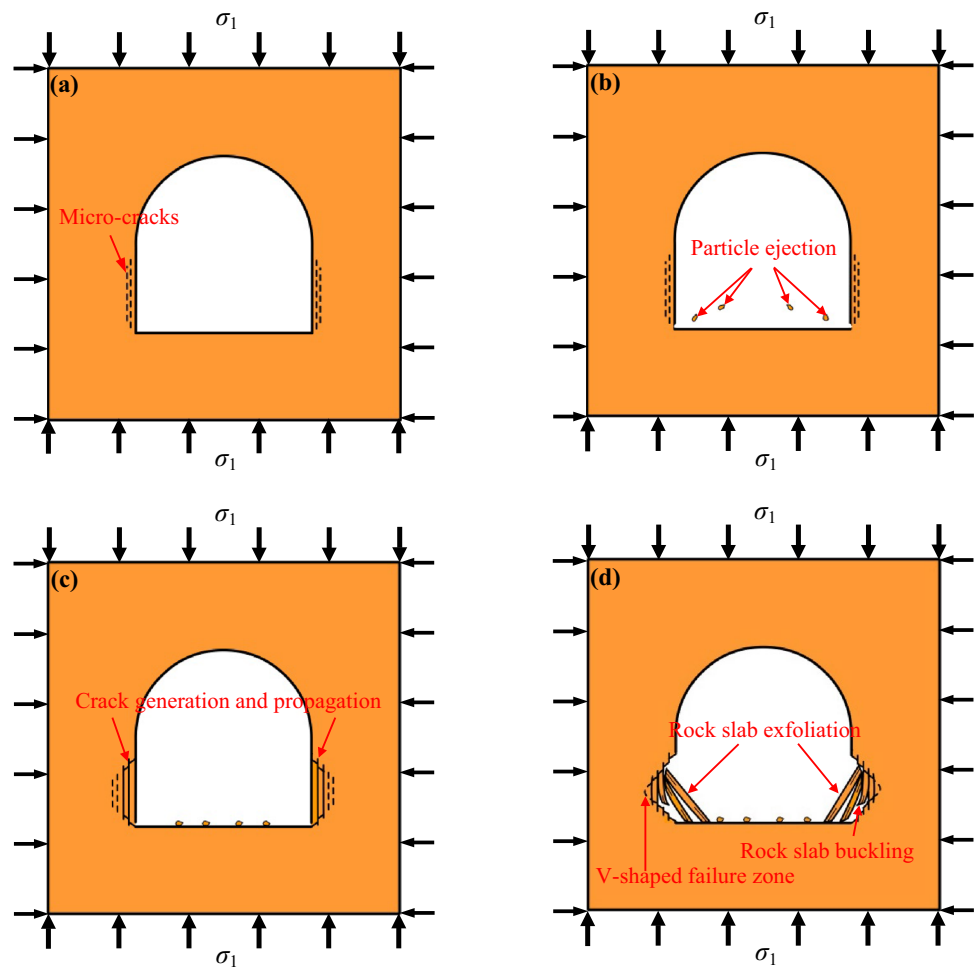


Table 3 Depth and location of the failure zone of sidewalls under different initial stress conditions^a

Specimen no.	σ_x (MPa)	σ_y (MPa)	Depth (mm)			Location (mm)		
			Left	Right	Average	Left	Right	Average
HZ-34-34	34.0	34.0	7.86	7.96	7.91	10.21	12.00	11.11
HZ-34-51	34.0	51.0	6.93	6.04	6.49	11.07	10.47	10.77
HZ-51-34	51.0	34.0	7.65	7.86	7.76	10.61	10.55	10.58
HZ-51-51	51.0	51.0	7.28	7.51	7.40	11.30	12.18	11.74

^aThe location of the failure zone is the vertical distance between the tip of the V-shaped failure zone and the floor

hole is 10.21–12.18 mm, which is 0.20–0.25 times the total tunnel height h (the distance from floor to roof). There is small variation in the position of the V-shaped notches; therefore, the horizontal stress has little effect on their positions. In addition, the failure zone under different stress conditions extends from the corner to the arch springing, and the stress state has no effect on the height of the V-shaped failure zone.

Figure 18 shows the failure severity of the D-shaped hole sidewall under four stress states when the vertical stress reached 140.0 MPa, 150.0 MPa, and 160.0 MPa,

respectively. When $\sigma_z = 140.0$ MPa, spalling failure occurred on both sidewalls of specimen HZ-34-34, and the right sidewall basically penetrated the whole specimen along the hole axis direction (Fig. 18a₁). There was slight failure on both sidewalls of specimens HZ-34-51 (Fig. 18b₁), HZ-51-34, (Fig. 18c₁) and HZ-51-51 (Fig. 18d₁), and the severity of the spalling failure was less than that of specimen HZ-34-34. The comparable results show that when the vertical stress is maintained at a high stress level, i.e., $\sigma_z = 140.0$ MPa, the lower the lateral stress, the more serious the spalling failure on both sidewalls of the D-shaped

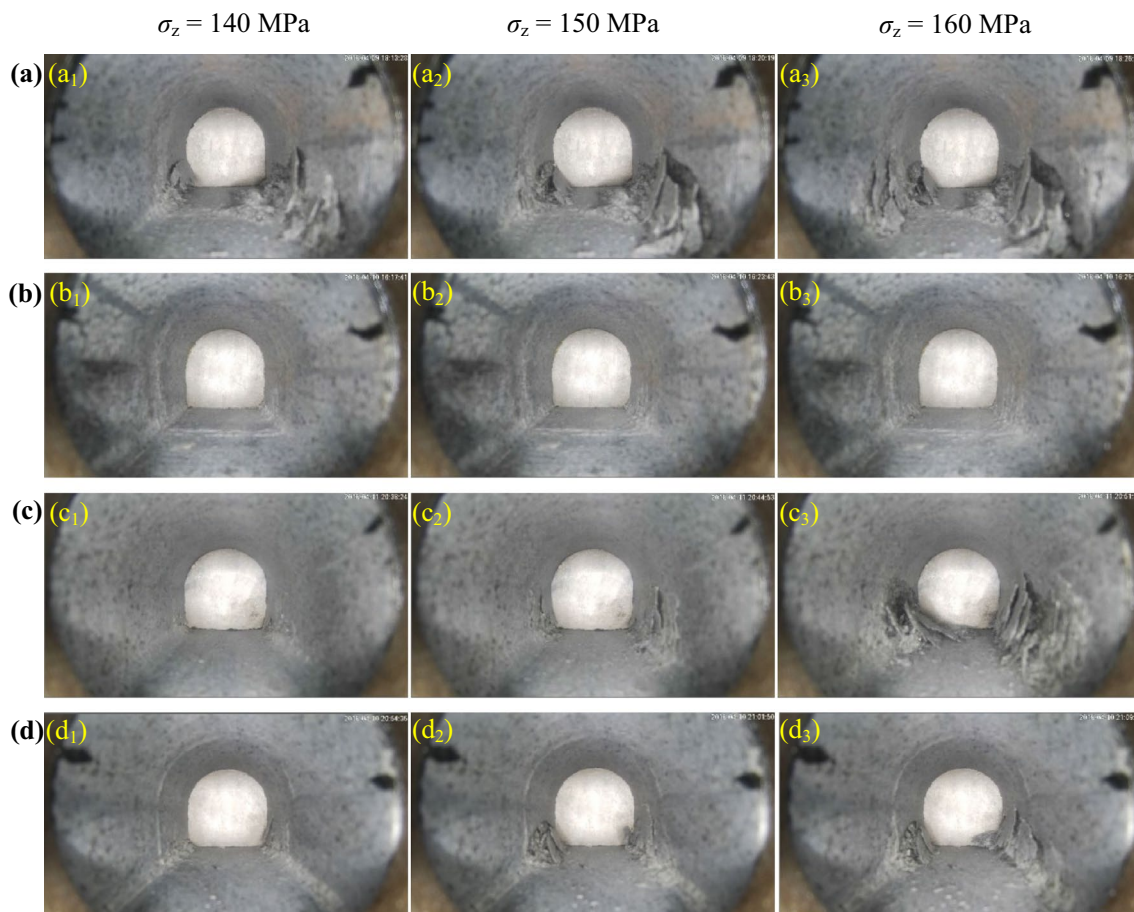


Fig. 18 Severity of spalling failure in a D-shaped tunnel under four stress states: **a** HZ-34-34, **b** HZ-34-51, **c** HZ-51-34, and **d** HZ-51-51

hole. When $\sigma_z = 150.0$ MPa, serious spalling failure occurred on both sidewalls of specimen HZ-34-34, as shown in Fig. 18a₂. From Fig. 18b₂, the failure on both sidewalls of specimen HZ-34-51 was very slight. Obvious spalling failure occurred on the left and right sidewalls of specimens HZ-51-34 (Fig. 18c₂) and HZ-51-51 (Fig. 18d₂), and the severity of spalling failure is basically similar; there is no obvious difference. Therefore, the same conclusion as for $\sigma_z = 140.0$ MPa can be obtained, which proves the repeatability of the above test result. When $\sigma_z = 160.0$ MPa, more severe spalling failure occurred on the left and right sidewalls of specimen HZ-34-34, as shown in Fig. 18a₃. It can be observed that the failure extent of the left sidewall is approximately two-thirds of the specimen axial length, while the failure of the right sidewall penetrated the specimen along the axial direction. Figure 18b₃ shows that the failure on both sidewalls of specimen HZ-34-51 was very slight. By comparing Fig. 18a₃ and b₃, it can be concluded that the spalling failure severity of the D-shaped hole sidewall is significantly reduced when σ_y is increased from 34.0 to 51.0 MPa, with $\sigma_x = 34.0$ MPa. From Fig. 18c₃, the spalling failure zone on the left sidewall is approximately half the axial length of the

specimen, and the spalling failure extended from the corner to the arch springing. Serious spalling failure occurred on the right sidewall, penetrating the specimen along the axis direction of the hole, and the cracks propagated to the arch springing. In Fig. 18d₃, the spalling failure zone on the left sidewall is also approximately half the axial length of the specimen. The spalling failure zone on the right sidewall is approximately two-thirds of the axial length of the specimen. Comparing Fig. 18c₃ and d₃, the spalling failure severity of the D-shaped hole sidewall is reduced when σ_y is increased from 34.0 to 51.0 MPa, with $\sigma_x = 51.0$ MPa. However, the reduction in the degree of spalling failure is much less than that for $\sigma_x = 34.0$ MPa. In summary, when the vertical stress is maintained at a high stress level and the horizontal axial stress remains unchanged, increasing the lateral stress can reduce the severity of the spalling failure of the D-shaped tunnel sidewall. The lower the horizontal axial stress is, the more obvious the reduction in the degree of the spalling failure of the surrounding rock is when the lateral stress increases by 17.0 MPa from 34.0 to 51.0 MPa. Therefore, when the horizontal axial stress is constant, the severity of the spalling failure can be reduced by strengthening support

to increase the lateral stress. The lower the horizontal axial stress, the more beneficial it is to reduce the severity of spalling damage. This has certain guiding significance for the design of D-shaped tunnel or cavern.

4.4 Influence of Tunnel Cross Section Shape on Surrounding Rock Failure

The geometry of the tunnel cross section, as an important parameter of structural design, has a significant impact on the safety and cost of tunnel engineering. Choosing a reasonable tunnel cross section is beneficial to reduce the likelihood of failure of tunnel surrounding rock and improve the stability of surrounding rock, which will increase the service life of the tunnel and save economic costs (Nakamura et al. 2003; Ren et al. 2005). In underground engineering design, D-shaped and circular cross section tunnels are often selected. To investigate the advantages and disadvantages of these two shapes, the test results of cubic granite specimens with D-shaped hole in this study were compared with those from experiments using cubic specimens (100 mm × 100 mm × 100 mm) with a Φ50 mm cylindrical hole from Gong et al. (2019a) and Si et al. (2018).

The initial failure stresses in the Z-direction (σ_{zi}) of the D-shaped holes and the circular holes under different stress conditions are listed in Table 4. The comparison of the initial failure stresses between the D-shaped holes and the circular holes is shown in Fig. 19. The initial failure stress of the D-shaped hole sidewall is significantly higher than that of the circular hole sidewall, which indicates that the stability limit of the D-shaped tunnel is higher than that of the circular tunnel. Therefore, the D-shaped tunnel should be applied to improve the bearing capacity of the surrounding rock in deep underground engineering. When the vertical stress is 140.0 MPa, the failure of the D-shaped and the circular hole sidewalls are shown in Fig. 20. From Fig. 20a, slight failure occurred in both sidewalls of the D-shaped hole, and no spalling structure was formed. However, for the circular tunnel cross section, a large number of rock fragments

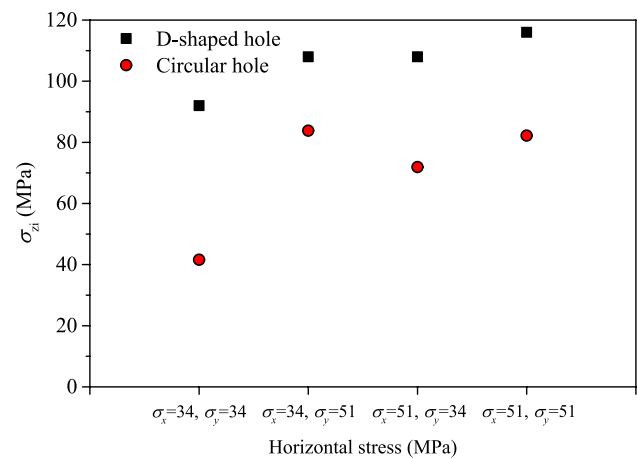


Fig. 19 Comparison of initial failure stress in the Z-direction (σ_{zi}) between D-shaped hole and circular hole

were quickly ejected, and both sidewalls experienced strong rockburst (see Fig. 20b). Comparing Fig. 20a and b, it is apparent that the D-shaped tunnel has better stability under the same 3D stress state. During the spalling failure process of the D-shaped hole sidewall, the rock slabs have no initial velocity when they are separated from the sidewall, and most of the rock fragments slide from the corner to the free surface, where the upper side of the rock slab leans on the sidewall. Therefore, the spalling failure of the sidewall is mainly characterized by static failure, while the rockburst of the sidewall of the circular hole is more severe, exhibiting dynamic failure. The main reason for this phenomenon is related to the size of the rock fragments and the energy accumulated by the surrounding rock. Figure 21 shows the rock fragments in the D-shaped hole and the circular hole. It can be seen that the rock fragments in the D-shaped hole are large and thick, showing slender plate shape, while the rock slabs in the circular hole are relatively small. Exfoliation of rock slab needs to consume high strain energy to transform into fracture surface energy, and the kinetic energy of rock slabs in the D-shaped hole is very small or even nonexistent. Therefore, it presents as static failure. In addition, from Fig. 21, the rock slabs produced by the two hole cross sections have similarities, that is, they are thick in the middle and thin at the edge.

The failure mode of the D-shaped hole is shown in Fig. 22a. Symmetrical V-shaped notches formed on both sidewalls. Similar to the D-shaped hole, an approximately symmetrical V-shaped notch is formed on both sidewalls of the circular hole, as shown in Fig. 22b. Comparing Fig. 22a and b, the V-shaped notches on both sidewalls of the D-shaped hole have a larger opening angle and width. Therefore, under a low-stress condition, the D-shaped cross section tunnel can be used to improve the stability of the surrounding rock. When the maximum principal stress (vertical

Table 4 Initial failure stress of D-shaped and circular holes under different stress conditions

Specimen no.	Horizontal stress (MPa)		σ_{zi} (MPa)	
	σ_x (MPa)	σ_y (MPa)	D-shaped hole	Circular hole (Gong et al. 2019a)
1	34.0	34.0	92.0	41.6
2	34.0	51.0	108.0	83.8
3	51.0	34.0	108.0	71.9
4	51.0	51.0	116.0	82.2

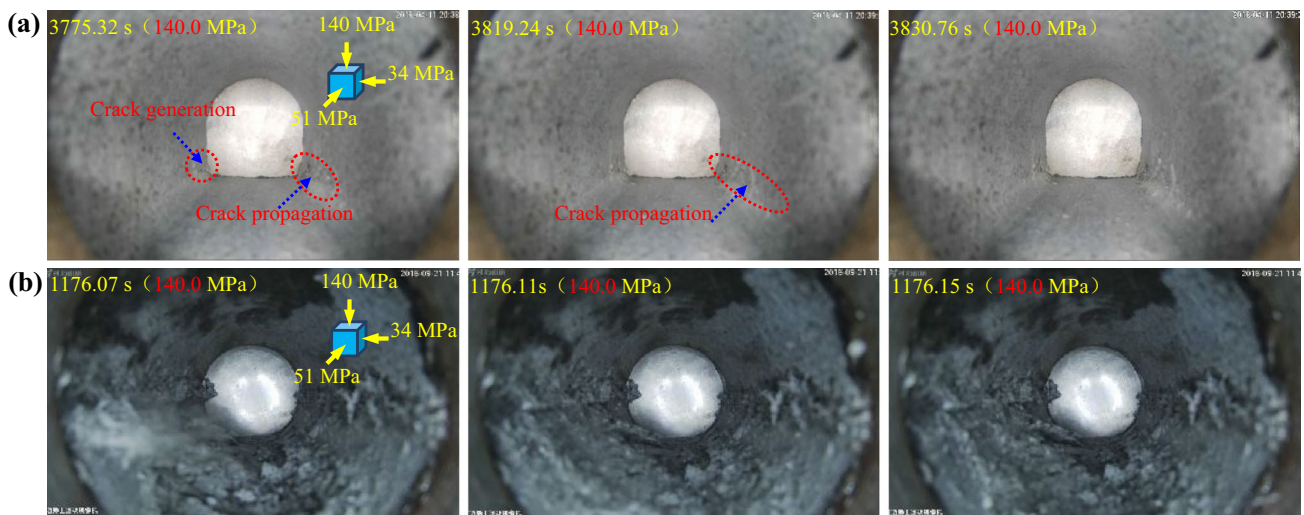


Fig. 20 Failure situations of sidewalls for D-shaped and circular holes: **a** D-shaped hole, **b** circular hole (Si et al. 2018)

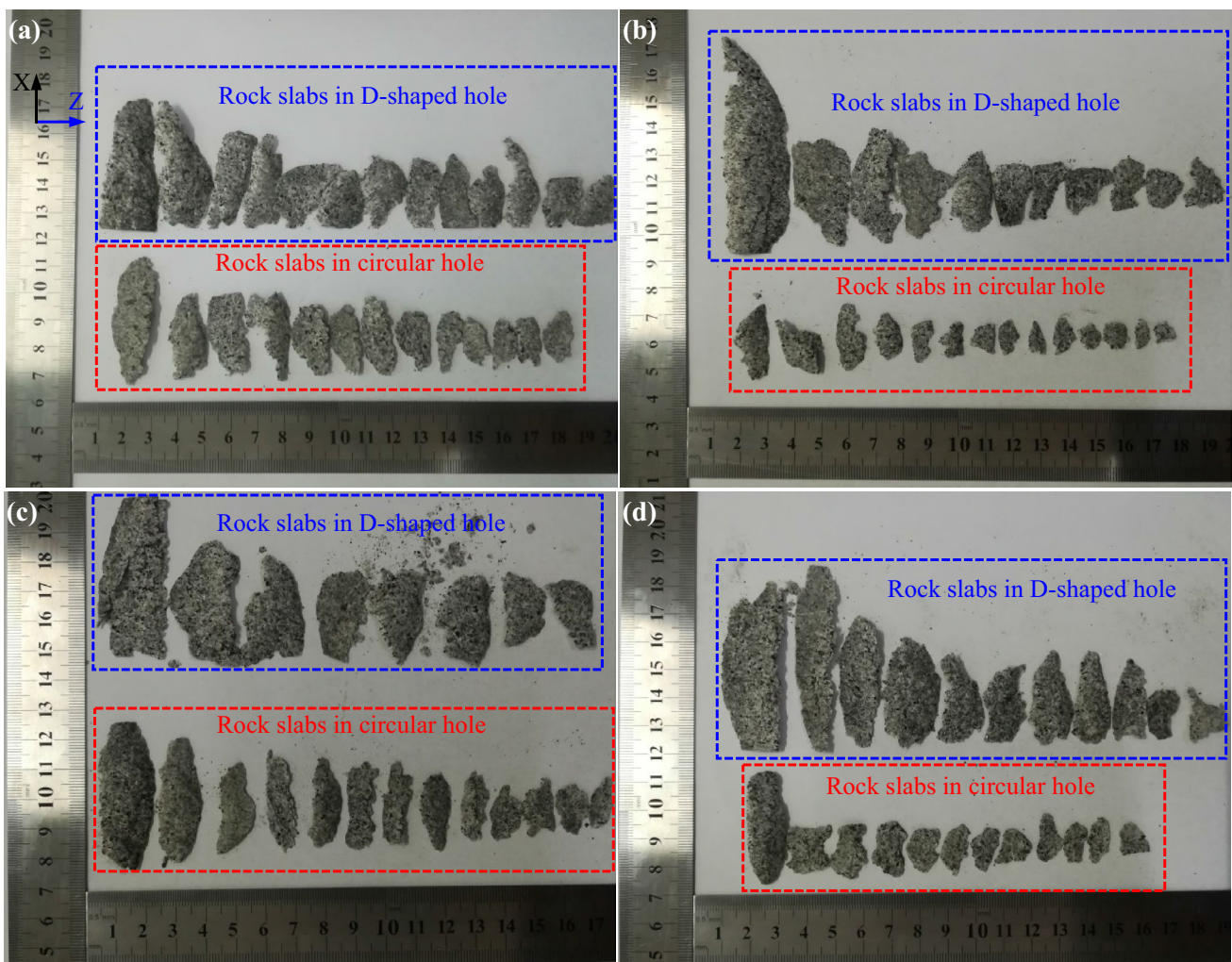


Fig. 21 Comparison of rock fragments damaged by surrounding rock of D-shaped and circular holes: **a** HZ-34-34 and HK-34-34, **b** HZ-34-51 and HK-34-51, **c** HZ-51-34 and HK-51-34, and **d** HZ-51-51 and HK-51-51

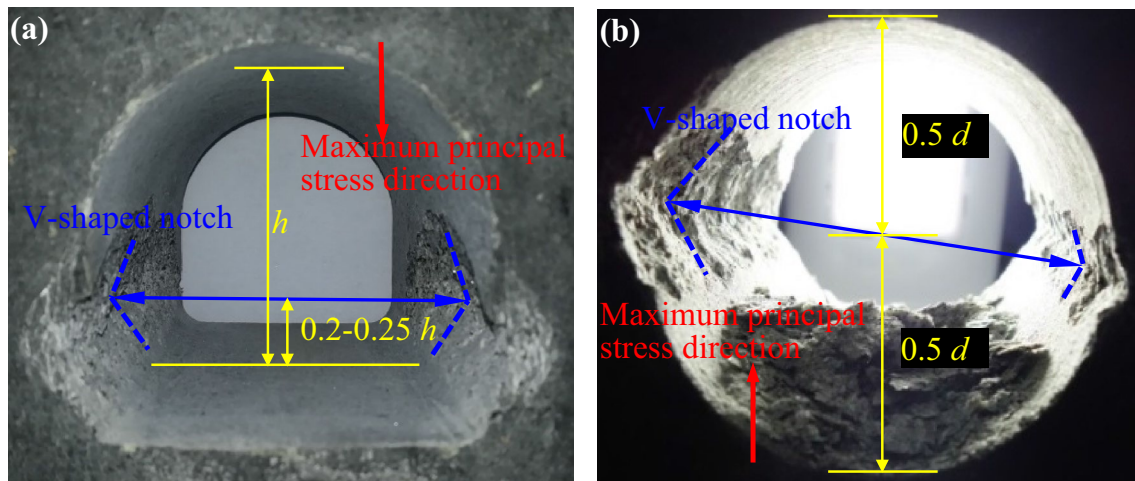


Fig. 22 Failure modes of sidewalls of D-shaped and circular holes: **a** D-shaped hole, **b** circular hole (Si et al. 2018)

stress) is high, the D-shaped tunnel suffers from serious spalling failure, and the failure range is wider than in the circular tunnel. From Fig. 22, the positions of the V-shaped notches are different. As described in Sect. 4.3, the position of the V-shaped notch tip is $0.20\text{--}0.25 h$ from the floor. However, the position of the V-shaped notch tip is $0.5 d$ (d is the diameter of the circular tunnel) from the floor in the circular tunnel. According to the position of the V-shaped notch, for the D-shaped cross section tunnel, the support should be strengthened on both sidewalls at the distance of $0.20\text{--}0.25 h$ from the floor to prevent the spalling failure of the surrounding rock. Because the depth of the failure zone is the largest, the bolt or cable used in the support should be longer than in other locations to have a better supporting effect. For the circular cross section tunnel, the support should be strengthened on both sidewalls at the distance of $0.5 d$ from the floor. Therefore, for tunnels with different cross sections, specific support design plans should be made according to the location and depth of the failure zone of the surrounding rock.

4.5 The Influence of Scale Effect

The scale effect is actually a common issue in the experimental studies of rock mechanical properties in the lab. In actual engineering, the tunnel size is generally large (in meters), so there is a problem of scale effect when rock specimens with small holes (generally tens of millimeters) are used to simulate the actual tunnel. When studying the specimen containing a hole, the specimen size should be 3–5 (or more) times the hole diameter. However, due to the limitation of test conditions, it is difficult to use hard rock materials to build tunnel models with the same size as the actual tunnels when carrying out tunnel test simulations indoors. Therefore, in the laboratory test simulation of

the tunnel, researchers mainly use the small scale hard rock model with holes. He et al. (2012, 2014) conducted simulation tests of rockbursts on $110\text{ mm} \times 110\text{ mm} \times 110\text{ mm}$ sandstone specimens contained a $\Phi 50\text{ mm}$ cylindrical hole under true-triaxial stress conditions, and during this investigation of the rockburst process, a broken band on the right sidewall of the circular hole was ultimately obtained. Gong et al. (2018a, 2019a) conducted rockburst simulation tests on Red Sandstone and fine-grained granite cubic specimens ($100\text{ mm} \times 100\text{ mm} \times 100\text{ mm}$) with 50 mm cylindrical holes under 3D high stress conditions, in which rockburst processes and symmetrical V-shaped notches were observed. Hu et al. (2019) carried out biaxial compression test on $200\text{ mm} \times 200\text{ mm} \times 200\text{ mm}$ sandstone specimens contained a $\Phi 78\text{ mm}$ cylindrical hole, and obtained that tensile cracks occupied most of the total micro-cracks, and tensile splitting dominated the failure process during the rockburst process. Kusui and Villaescusa (2016, 2018) carried out two-dimensional loading tests on sandstone specimens ($400\text{ mm} \times 400\text{ mm} \times 200\text{ mm}$) with a $\Phi 200\text{ mm}$ cylindrical hole, and observed spalling failure and rockburst of the hole sidewall. For the above studies, small scale specimens were used to conduct simulation tests, and the ratio of the specimen size to the hole diameter was 2.2 (He et al. 2012, 2014), 2.0 (Gong et al. 2018a, 2019a), 2.56 (Hu et al. 2019), and 2.0 (Kusui and Villaescusa 2016, 2018), respectively. Although scale effect existed, they all achieved the effect of simulating rockburst or spalling, and some useful conclusions were obtained. Wu et al. (2020) discussed the scale effect, and thought that although the scale of the cubic specimens was small, the test results can help us to understand and recognize the failure process of the sidewalls of holes in deep underground engineering. In this study, similar idea is adopted in the experimental tests considering the available testing conditions.

In this study, the test results are as listed in Table 4. The stress conditions for initial spalling failure of D-shaped holes are $\sigma_{zi}/\sigma_c \approx 0.35 \sim 0.44$. However, a large number of studies have demonstrated that the field strength of the rock mass is approximately half of the laboratory uniaxial compressive strength (Stacey 1981; Pelli et al. 1991; Myrvang 1991; Martin 1995). Therefore, when the test results are applied to the field, the stress condition ($\sigma_{zi}/\sigma_c \approx 0.35 \sim 0.44$) should be changed to $\sigma_1/\sigma_c \approx 0.175 \sim 0.22$ (σ_1 is the far-field maximum stress in the field). Some scholars have conducted in situ observation of spalling failure in underground tunnels or caverns. For example, Ortlepp et al. (1976) compiled experience from tunnels in brittle rocks in South African gold mines and suggested that the stability of these tunnels could be assessed using the ratio of the far-field maximum stress (σ_1) to the laboratory uniaxial compressive strength (σ_c), and indicated that spalling failure occurs when $\sigma_1/\sigma_c > 0.2$. Hoek and Brown (1980) conducted field observations of underground mines in South Africa and pointed out that spalling failure can be observed when $\sigma_1/\sigma_c = 0.2$. In the southwest of China, spalling failure occurred during the excavation of the large underground powerhouse at a hydropower station under construction ($\sigma_1 = 25 \sim 30$ MPa, $\sigma_3 = 13 \sim 15$ MPa, $\sigma_c = 135$ MPa, $\sigma_1/\sigma_c = 0.19 \sim 0.22$) (Liu et al. 2017). From the above analysis, it can be found that both results can be considered basically consistent. Therefore, the converted test results ($\sigma_1/\sigma_c \approx 0.175 \sim 0.22$) can be applied to roughly assess the spalling failure of the on-site tunnels.

Although the scale effect may affect the deformation of the hole, the test results are basically consistent with the in situ spalling failure of D-shaped tunnel (Sect. 4.1). Therefore, the research can help us to understand the failure process of D-shaped tunnel in underground engineering, progressive evolution process and mechanism of spalling, and can provide reference and guidance for the design (optimization of cross section shape and excavation direction) and spalling prevention of hard rock tunnels. In the future, once the capacities of the true-triaxial testing machines meet the requirements of testing the large-scale specimens, larger rock specimens can be used in the tests so as to minimize the scale effect and better observe the spalling failure process of the specimen.

5 Conclusions

In this study, the spalling failure process and mechanism in D-shaped cross section tunnel were investigated by conducting true-triaxial loading tests on cubic granite specimens with a through D-shaped hole. The spalling failure process was monitored and recorded in real time using a wireless microcamera. By analyzing the experimental results, the following primary conclusions can be obtained:

- (1) During the test, the whole specimens remained stable, and only the sidewall experienced spalling failure. The spalling failure exhibits tensile failure characteristics, and it is approximately parallel to the tunnel sidewall or maximum principal stress, which is consistent with the spalling failure in situ observed in underground engineering.
- (2) The spalling failure process of the D-shaped hole sidewall can be divided into four periods: calm period, fine particle ejection period, crack generation and propagation period, and rock slab gradually buckling and spalling period. The spalling failure process of the sidewall is relatively slow and takes a long time; during this process, other locations on both sidewalls experience particle ejection, crack generation, and crack propagation. After layer-by-layer rock slab spalling, symmetrical V-shaped notches form on the left and right sidewalls, and the scope of the V-shaped notches is from the corner to the arch springing of the D-shaped hole.
- (3) The stress state in the horizontal directions (axial and lateral) has a significant effect on the severity of spalling failure of the D-shaped hole sidewall for a given vertical stress. When the vertical stress is maintained at a high stress level and the horizontal axial stress is constant, increasing the lateral stress can reduce the severity of the spalling failure of the hole sidewall. The higher the lateral stress is, the shallower the depth of the V-shaped notch is. When the horizontal axial stress is low, the lateral stress increases by 17.0 MPa from 34.0 to 51.0 MPa, and the depth of the V-shaped notch decreases more obviously. In addition, the range of the V-shaped notch is not affected by the horizontal stress state (horizontal axial stress and lateral stress).
- (4) Comparing the sidewall failure of the D-shaped and circular holes, the initial failure stress of the D-shaped hole sidewall is significantly higher than that of the circular hole sidewall. Therefore, the D-shaped tunnel should be applied to improve the stability of the surrounding rock in deep underground engineering. In addition, rock slabs in the D-shaped hole are large and thick with slender plate shape, whereas the rock slabs in the circular hole are relatively small. The rock slabs also have some similarities, that is, they are thick in the middle and thin at the edge. The rock slab produced by the D-shaped hole sidewall has no initial velocity and represents static failure. However, rockburst occurred in the circular hole, with a strong dynamic characteristic.
- (5) For tunnels of different geometries, the positions of the V-shaped notches are different. When the maximum principal stress is parallel to the vertical direction, for the D-shaped cross section tunnel, the position of the

V-shaped notch tip is 0.20–0.25 h above the floor; for the circular cross section tunnel, the position of the V-shaped notch tip is 0.5 d above the tunnel floor. Therefore, for tunnels with different cross sections, specific support design plans should be made according to the location and depth of the failure zone of the surrounding rock.

Acknowledgements This work was supported by the National Natural Science Foundation of China (Grant No. 41630642 and 51904335), and the Fundamental Research Funds for the Central Universities of Central South University (Grant No. 2019zzts310).

Compliance with Ethical Standards

Conflict of interest The authors declare that they have no conflict of interest.

References

- Bobet A, Einstein HH (1998) Fracture coalescence in rock-type materials under uniaxial and biaxial compression. *Int J Rock Mech Min Sci* 35(7):863–888
- Brown ET, Hoek E (1978) Trends in relationships between measured in-situ stresses and depth. *Int J Rock Mech Min Sci Geomech Abstr* 15(4):211–215
- Cai M (2008) Influence of intermediate principal stress on rock fracturing and strength near excavation boundaries—insight from numerical modeling. *Int J Rock Mech Min Sci* 45(5):763–772
- Cai M, Kaiser PK, Martin CD (1998) A tensile model for the interpretation of microseismic events near underground openings. *Pure Appl Geophys* 153(1):67–92
- Cheon DS, Jeon S, Park C, Ryu C (2006) An experimental study on the brittle failure under true triaxial conditions. *Tunn Undergr Space Technol* 21(3–4):448–449
- Cheon DS, Jeon S, Park C, Song WK, Park ES (2011) Characterization of brittle failure using physical model experiments under polyaxial stress conditions. *Int J Rock Mech Min Sci* 48(1):152–160
- Diederichs MS (2007) The 2003 Canadian Geotechnical Colloquium: Mechanistic interpretation and practical application of damage and spalling prediction criteria for deep tunnelling. *Can Geotech J* 44(9):1082–1116
- Dowding CH, Andersson CA (1986) Potential for rock bursting and slabbing in deep caverns. *Eng Geol* 22(3):265–279
- Du K, Tao M, Li XB, Zhou J (2016) Experimental study of slabbing and rockburst induced by true-triaxial unloading and local dynamic disturbance. *Rock Mech Rock Eng* 49(9):3437–3453
- Feng XT, Haimson B, Li XC, Chang CD, Ma XD, Zhang XW, Ingraham M, Suzuki K (2019) ISRM Suggested Method: determining deformation and failure characteristics of rocks subjected to true triaxial compression. *Rock Mech Rock Eng* 52(6):2011–2020
- Feng XT, Xu H, Qiu SL, Li SJ, Yang CX, Guo HS, Cheng Y, Gao YH (2018) In situ observation of rock spalling in the deep tunnels of the China Jinping Underground Laboratory (2400 m depth). *Rock Mech Rock Eng* 51(4):1193–1213
- Gay NC (1976) Fracture growth around openings in large blocks of rock subjected to uniaxial and biaxial compression. *Int J Rock Mech Min Sci Geomech Abstr* 13(8):231–243
- Gong FQ, Luo Y, Li XB, Si XF, Tao M (2018a) Experimental simulation investigation on rockburst induced by spalling failure in deep circular tunnels. *Tunn Undergr Space Technol* 81:413–427
- Gong FQ, Si XF, Li XB, Wang SY (2019a) Experimental investigation of strain rockburst in circular caverns under deep three-dimensional high stress conditions. *Rock Mech Rock Eng* 52(5):1459–1474
- Gong FQ, Wu WX, Li TB, Si XF (2019b) Experimental simulation and investigation of spalling failure of rectangular tunnel under different three-dimensional stress states. *Int J Rock Mech Min Sci* 122:104081
- Gong FQ, Yan JY, Li XB (2018b) A new criterion of rock burst proneness based on the linear energy storage law and the residual elastic energy index. *Chin J Rock Mech Eng* 37(9):1993–2014
- Gong FQ, Yan JY, Li XB, Luo S (2019c) A peak-strength strain energy storage index for rock burst proneness of rock materials. *Int J Rock Mech Min Sci* 117:76–89
- Gong QM, Yin LJ, Wu SY, Zhao J, Ting Y (2012) Rock burst and slabbing failure and its influence on TBM excavation at headrace tunnels in Jinping II hydropower station. *Eng Geol* 124(1):98–108
- Haimson B (2007) Micromechanisms of borehole instability leading to breakouts in rocks. *Int J Rock Mech Min Sci* 44(2):157–173
- He MC, Liu DQ, Gong WL, Wang CC, Kong J, Du S, Zhang S (2014) Development of a testing system for impact rockbursts. *Chin J Rock Mech Eng* 39(9):1729–1739
- He MC, Xia HM, Jia XN, Gao WL, Zhao F, Liang KY (2012) Studies on classification, criteria, and control of rockbursts. *J Rock Mech Geotech Eng* 4(2):97–114
- Hidalgo KP, Nordlund E (2012) Failure process analysis of spalling failure—comparison of laboratory test and numerical modelling data. *Tunn Undergr Space Technol* 32:66–77
- Hoek E, Brown ET (1980) *Underground excavations in rock*. The Institution of Mining and Metallurgy, London
- Hu XC, Su GS, Chen GY, Mei SM, Feng XT, Mei GX, Huang XH (2019) Experiment on rockburst process of borehole and its acoustic emission characteristics. *Rock Mech Rock Eng* 52:783–802
- Jia P, Yang TH, Yu QL (2012) Mechanism of parallel fractures around deep underground excavations. *Theor Appl Fract Mech* 61:57–65
- Jiang Q, Feng XT, Fan YL, Fan QX, Liu GF, Pei SF, Duan S (2017) In situ experimental investigation of basalt spalling in a large underground powerhouse cavern. *Tunn Undergr Space Technol* 68:82–94
- Jiang Q, Feng XT, Xiang TB, Su GS (2010) Rockburst characteristics and numerical simulation based on a new energy index: a case study of a tunnel at 2500 m depth. *Bull Eng Geol Environ* 69(3):381–388
- Kusui A, Villaescusa E (2016) Seismic response prior to spalling failure in highly stressed underground tunnels. In: *Proceedings of the Seventh International Conference & Exhibition on Mass Mining*, Sydney, Australia.
- Li XB, Feng F, Li DY, Du K, Ranjith PG, Rostami J (2018a) Failure characteristics of granite influenced by sample height-to-width ratios and intermediate principal stress under true-triaxial unloading conditions. *Rock Mech Rock Eng* 51(5):1321–1345
- Li XB, Gong FQ, Tao M, Dong LJ, Du K, Ma CD, Zhou Z, Yin TB (2017) Failure mechanism and coupled static-dynamic loading theory in deep hard rock mining: a review. *J Rock Mech Geotech Eng* 9(4):767–782
- Li XB, Wang SF, Wang SY (2018b) Experimental investigation of the influence of confining stress on hard rock fragmentation using a conical pick. *Rock Mech Rock Eng* 51(1):255–277
- Liu GF, Feng XT, Jiang Q, Yao ZB, Li SJ (2017) In situ observation of spalling process of intact rock mass at large cavern excavation. *Eng Geol* 226:52–69

- Luo Y (2020) Influence of water on mechanical behavior of surrounding rock in hard-rock tunnels: An experimental simulation. *Eng Geol* 277:105816
- Luo Y, Gong FQ, Li XB, Wang SY (2020) Experimental simulation investigation of influence of depth on spalling characteristics in circular hard rock tunnel. *J Cent South Univ* 27(3):891–910
- Martin CD (1995) Brittle rock strength and failure: Laboratory and in situ. In *Proceedings of the 8th, ISRM Congress on Rock Mechanics*, A.A. Balkema, Rotterdam, pp 1033–1040
- Martin CD (1997) Seventeenth Canadian geotechnical colloquium: the effect of cohesion loss and stress path on brittle rock strength. *Can Geotech J* 34(5):698–725
- Martin CD, Read RS, Martino JB (1997) Observations of brittle failure around a circular test tunnel. *Int J Rock Mech Min Sci* 34(7):1065–1073
- Myrvang AM (1991) Estimation of in situ compressive strength of rocks from in situ stress measurements in highly stressed rock structures. In *Proceedings of the 7th ISRM Congress on Rock Mechanics*, A.A. Balkema, Rotterdam, pp 573–575
- Nakamura H, Kubota T, Furukawa M, Nakao T (2003) Unified construction of running track tunnel and crossover tunnel for subway by rectangular shape double track cross-section shield machine. *Tunn Undergr Space Technol* 18(2–3):253–262
- Ortlepp WD, O’Ferrall RCM, Wilson JW (1976) Support methods in tunnels. *Association of Mine Managers of South Africa, Papers and Discussion*, pp 167–195
- Ortlepp WD, Stacey TR (1994) Rockburst mechanisms in tunnels and shafts. *Tunn Undergr Space Technol* 9(1):59–65
- Pelli F, Kaiser PK, Morgenstern NR (1991) An interpretation of ground movements recorded during construction of the Donkin-Morien tunnel. *Can Geotech J* 28(2):239–254
- Pinto C, Fonseca J (2013) Mechanical behavior of high strength granite for new prestressed stone structures. *Int J Rock Mech Min Sci* 60:452–460
- Qiu JD, Luo L, Li XB, Li DY, Chen Y, Luo Y (2020) Numerical investigation on the tensile fracturing behavior of rock-shotcrete interface based on discrete element method. *Inter J Min Sci Technol* 30:293–301
- Qiu SL, Feng XT, Zhang CQ, Xiang TB (2014) Estimation of rockburst wall-rock velocity invoked by slab flexure sources in deep tunnels. *Can Geotech J* 51(5):520–539
- Ren G, Smith JV, Tang JW, Xie YM (2005) Underground excavation shape optimization using an evolutionary procedure. *Comput Geotech* 32(2):122–132
- Sagong M, Park D, Yoo J, Lee JS (2011) Experimental and numerical analyses of an opening in a jointed rock mass under biaxial compression. *Int J Rock Mech Min Sci* 48(7):1055–1067
- Si XF, Gong FQ (2020) Strength-weakening effect and shear-tension failure mode transformation mechanism of rockburst for fine-grained granite under triaxial unloading compression. *Int J Rock Mech Min Sci* 131:104347
- Si XF, Gong FQ, Luo Y, Li XB (2018) Experimental simulation on rockburst process of deep three-dimensional circular cavern. *Rock Soil Mech* 39(2):621–634
- Stacey TR (1981) A simple extension strain criterion for fracture of brittle rock. *Int J Rock Mech Min Sci Geomech Abstr* 18(6):469–474
- Stephansson O, Särkkä P, Myrvang A (1986) State of stress in Fenoscandia. In: *Proceedings on rock stress and rock stress measurement*, Stockholm, pp 21–32
- Villaescusa E, Kusui A (2018) Evaluating the performance of high energy dissipation capacity surface support systems. In: *Proceedings of International Symposium on Earth Science & Technology*, Kyushu, Japan
- Wang SF, Huang LQ, Li XB (2020) Analysis of rockburst triggered by hard rock fragmentation using a conical pick under high uniaxial stress. *Tunn Undergr Space Technol* 96:103195
- Wu WX, Gong FQ, Yang WM (2020) Experimental simulation study of spalling in deep rectangular tunnel with plastic fine grain marble. *Tunn Undergr Space Technol* 98:103319
- Zhou H, Lu JJ, Xu RC, Zhang CQ, Meng FZ (2016) Critical problems of study of slabbing failure of surrounding rock in deep hard rock tunnel and research progress. *Rock Soil Mech* 36(10):2737–2749

Publisher’s Note Springer Nature remains neutral with regard to jurisdictional claims in published maps and institutional affiliations.